Decoupling of Magnetic Fabrics From Magnetic Remanences: Insights From Migmatites in Central Tianshan, NW China

Xin Zhu, Bo Wang, Yunpeng Dong, Yan Chen, Hongsheng Liu, Shengsi Sun, Zhenhua Xue, Lingling Zhong, Zhiyuan He

JGR Solid Earth

RESEARCH ARTICLE
10.1029/2024JB029473

Decoupling of Magnetic Fabrics From Magnetic Remanences: Insights From Migmatites in Central Tianshan, NW China

Xin Zhu[1,2,3], Bo Wang[2], Yunpeng Dong[1], Yan Chen[3], Hongsheng Liu[4], Shengsi Sun[1], Zhenhua Xue[5], Lingling Zhong[6], and Zhiyuan He[7]

[1]State Key Laboratory of Continental Dynamics, Department of Geology, Northwest University, Xi'an, China, [2]State Key Laboratory for Mineral Deposits Research, School of Earth Sciences and Engineering, Nanjing University, Nanjing, China, [3]Institut des Sciences de la Terre d'Orléans, Université d'Orléans, CNRS/INSU, Orléans, France, [4]School of Resources Environment and Safety Engineering, University of South China, Hengyang, China, [5]School of Earth Sciences, China University of Geosciences, Wuhan, China, [6]College of Earth Sciences, Chengdu University of Technology, Chengdu, China, [7]Laboratory for Mineralogy and Petrology, Department of Geology, Ghent University, Ghent, Belgium

Abstract The coupling of magnetic fabrics and magnetic remanences is critical in interpreting paleomagnetic data. To estimate whether primary magnetic fabrics imply primary magnetic remanences, and to assess the practicability of metamorphic rocks in magnetic study, we carried out petrographic, geochronological, rock magnetic investigations, and analyses in anisotropy of magnetic susceptibility and paleomagnetism on migmatites in the Central Tianshan, NW China. Petrological observations indicate no significant dynamic recrystallization post to the migmatization. In-situ monazite U-Pb dating suggests that the migmatization happened during ~314–297 Ma. Rock magnetic results reveal that the magnetic properties of migmatites are dominated by biotites with minor titanomagnetites. Despite the structural and compositional complexities of migmatites, a simple magnetic fabric pattern is observed with concentrated magnetic foliations and dispersed magnetic lineations. The anisotropy degree and shape parameter significantly change from leucosomes, mesosomes to melanosomes, suggesting that the magnetic fabrics should have been acquired during the migmatization. Characteristic remanent magnetization directions were isolated from a quarter of samples with anomalous shallow magnetic inclination. Combined with available geochronological and paleomagnetic results from the Central Tianshan and neighboring blocks, the magnetic remanences preserved in the migmatites were suggested to be obtained at ~314–303 Ma, later than the acquisition of magnetic fabrics, probably due to thermal remagnetization or resulted from long-term progressive magnetization during tectonic exhumation of migmatites. This study provides an important yet rarely reported example to manifest the decoupling of magnetic fabrics from magnetic remanences. Meanwhile, migmatites are found to be operable materials for magnetic fabric and paleomagnetic studies.

Plain Language Summary The magnetic fabric and the magnetic remanence are widely utilized to resolve various geoscience problems. Available studies suggest that the coupling of magnetic fabrics and magnetic remanences is crucial to constrain the relative magnetic remanence age for further paleomagnetic interpretation. Meanwhile, metamorphic rocks have barely been investigated from magnetic perspectives so far. To judge whether primary magnetic fabrics imply primary magnetic remanences, and to evaluate the applicability of magnetic methods on metamorphic rocks, we carried out a multidisciplinary study on the migmatites in the Central Tianshan, NW China. Our study found that the migmatites demonstrate a simple magnetic fabric pattern with a horizontal and oblate geometry. Their magnetic fabrics should have been acquired during the migmatization process at ~314–297 Ma. However, the magnetic remanences carried by the migmatites were obtained later than the acquisition of the magnetic fabrics probably due to thermal remagnetization or long-term magnetization during tectonic exhumation of the migmatites. This study provides an important yet few reported example showing the decoupling of magnetic fabrics from magnetic remanences, indicating that primary magnetic fabrics do not necessarily indicate primary, or at least contemporaneous, magnetic remanences. Moreover, migmatites are found to be practicable objects for magnetic fabric and paleomagnetic studies.

Key Points:

- The magnetic fabrics of the Baluntai migmatites in the Central Tianshan were acquired during the migmatization process at ~314–297 Ma
- The magnetic remanences of the Baluntai migmatites were obtained later than the acquisition of the magnetic fabrics
- We report the decoupling of magnetic fabrics from magnetic remanences and indicate migmatites are operable materials for magnetic studies

Supporting Information:

Supporting Information may be found in the online version of this article.

Correspondence to:

B. Wang and Y. Dong,
bwang@nju.edu.cn;
dongyp@nwu.edu.cn

Citation:

Zhu, X., Wang, B., Dong, Y., Chen, Y., Liu, H., Sun, S., et al. (2025). Decoupling of magnetic fabrics from magnetic remanences: Insights from migmatites in central Tianshan, NW China. *Journal of Geophysical Research: Solid Earth*, *130*, e2024JB029473. https://doi.org/10.1029/2024JB029473

Received 6 MAY 2024
Accepted 22 DEC 2024

Author Contributions:

Conceptualization: Xin Zhu, Bo Wang, Yan Chen
Data curation: Yan Chen
Formal analysis: Xin Zhu, Hongsheng Liu
Funding acquisition: Xin Zhu, Bo Wang, Yunpeng Dong
Investigation: Xin Zhu, Yan Chen, Hongsheng Liu, Zhenhua Xue
Methodology: Xin Zhu, Yan Chen
Project administration: Yan Chen
Supervision: Bo Wang, Yunpeng Dong, Yan Chen
Validation: Bo Wang, Yunpeng Dong
Writing – original draft: Xin Zhu
Writing – review & editing: Bo Wang, Yunpeng Dong, Yan Chen, Shengsi Sun, Zhenhua Xue, Lingling Zhong, Zhiyuan He

1. Introduction

The magnetic properties of rocks are used as crucial information to resolve specific geoscience problems. For example, the magnetic remanence is powerful in understanding the paleomagnetic field that offers one of the few glimpses of the past of the Earth (i.e., Paleomagnetism), providing essential quantitative constraints on kinematics of tectonic plates (e.g., Cheng et al., 2023; Patzelt et al., 1996), paleogeography (e.g., Huang et al., 2018; Torsvik et al., 2012), and geodynamics (e.g., Mitchell et al., 2021; Tarduno et al., 2023). In addition, the magnetic fabric affords the possibility for (semi-)quantitative study about deformation intensity and geometry, enabling applications in terms of paleomagnetic interpretation (e.g., Chen et al., 2004; Raposo et al., 2003), emplacement mode of magmatic intrusive bodies (e.g., Charles et al., 2009; Liu et al., 2023), and globally significant tectonics (e.g., S. H. Li et al., 2020; Xue et al., 2022; Wei et al., 2023).

The magnetic fabric, also called the anisotropy of magnetic susceptibility (AMS), has since long been used to constrain the relative magnetic remanence age for further paleomagnetic interpretation (Rochette et al., 1992). Primary remanences are usually found in sedimentary and volcanic sequences that keep their original fabrics (e.g., Bian et al., 2022; Huang et al., 2019; Sun et al., 2012; Yuan et al., 2023; Zhan et al., 2007; Zhao et al., 2020; Zhu et al., 2019). Besides, weakly deformed rocks with "pencil structure" to "weak cleavage" magnetic fabrics (Hrouda & Chadima, 2020; S. H. Li et al., 2020) are possible to retain primary remanence information (e.g., Cheng et al., 2023; S. H. Li et al., 2020; Kligfield et al., 1983; Wang, Yang, et al., 2022; Wen et al., 2013; Yi et al., 2015). Moreover, overprinted magnetic fabrics in more intensively deformed rocks are utilized as an argument to eliminate primary magnetic remanences (e.g., Jing et al., 2015; Zhao et al., 2014). Thus, the primary magnetic fabric may be deemed to be a clue to the primary remanence. To verify whether this conclusion is valid, counter-examples, if any, are important that rocks carry decoupled magnetic fabrics and magnetic remanences, yet few have been reported.

Metamorphic rocks are usually less studied in paleomagnetism largely for their complicated isotopic ages and the multi-component nature of the characteristic remanent magnetizations (ChRMs) (Pesonen et al., 2021). However, some researchers suggested that high-grade metamorphic rocks could be suitable for paleomagnetic studies by correcting the effect of magnetic anisotropy on paleomagnetic directions (e.g., D'Agrella-Filho et al., 2004; Raposo et al., 2003). Such a dilemma is mainly because the timings and relationship between magnetic fabrics and magnetic remanences are difficult to determine for metamorphic rocks. As a kind of amphibolite-facies high-grade metamorphic rocks, migmatites were barely studied for the magnetic fabric due to their structural and compositional complexities acquired under partially melted conditions (Ferré et al., 2003, 2004), although a few studies indicated that the AMS could be applied to understand the formation mechanism of migmatites, the regional tectonic evolution history, and even the bulk deformation and rheology of the lower to middle continental crust (e.g., Charles et al., 2009; Ferré et al., 2003; Kruckenberg et al., 2010; Schulmann et al., 2009). Apparently, more work is necessary to further test the practicability of migmatites in paleomagnetic research by exploring the relationship between magnetic fabrics and magnetic remanences.

In this study, we focus on the Baluntai area of Central Tianshan (NW China) as migmatites are well-developed (Figures 1 and 2; XBGMR, 1993). We conducted comprehensive petrographic observations, rock magnetic and geochronological investigations, as well as magnetic fabric and paleomagnetic analyses on the Baluntai migmatites, aiming to answer the question of whether primary magnetic fabrics imply primary magnetic remanences and to evaluate if migmatites are operable materials for magnetic fabric and paleomagnetic studies.

2. Geological Background and Sampling

2.1. Regional Geological Background

Located in the southwestern part of the Central Asian Orogenic Belt (CAOB; Jahn et al., 2000) or the Altaïds (Sengör et al., 1993; Xiao et al., 2015), the Tianshan Orogenic Belt, extending over 2,500 km from NW China to Uzbekistan, is one of the most spectacular orogens in the world (Figures 1a and 1b; Alexeiev et al., 2015; Allen et al., 1993; Shu et al., 2004; Wang, Song, et al., 2022). Within the Chinese territory, the Tianshan belt is subdivided into four tectonic units, namely, from north to south, the North Tianshan, the Yili Block, the Central Tianshan, and the South Tianshan. Generally, these units are separated from each other by major strike-slip faults that reworked the ancient suture zones (Figure 1b; Gao et al., 1998; Han et al., 2011; Han & Zhao, 2018; He et al., 2021; Wang et al., 2006).

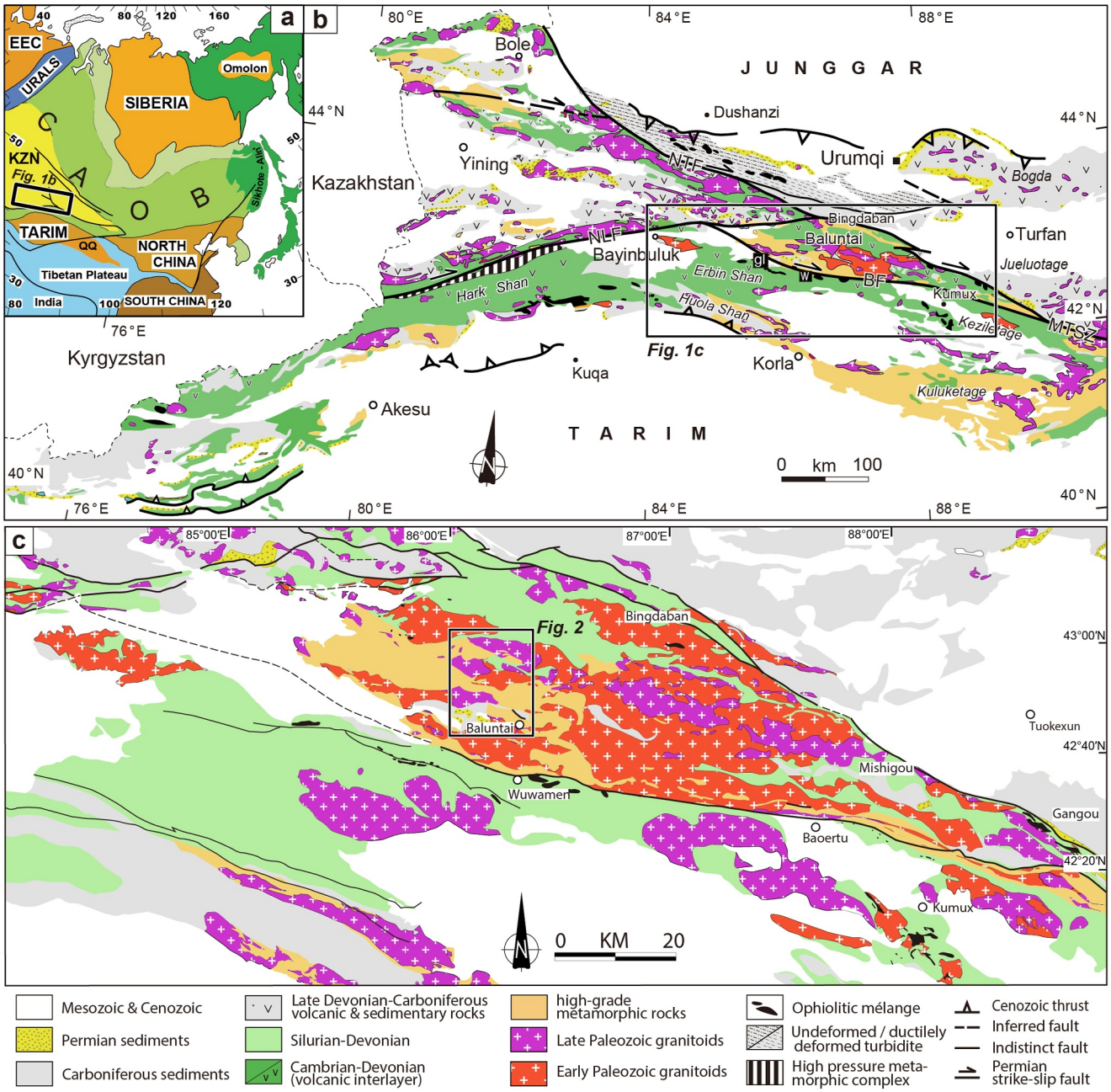

Figure 1. (a) Simplified tectonic division of the eastern Asia (after Jahn et al., 2000). EEC, East European Craton; KZN, Kazakhstan; QQ, Qaidam-Qilian. (b) Tectonic division of the Chinese segment of the Tianshan orogen (modified from XBGMR, 1993; Wang et al., 2018). Abbreviations of the faults and localities cited in the text: NTF, North Tianshan Fault; NLF, Nalati Fault; MTSZ, Middle Tianshan Shear Zone; BF, Baluntai Fault; gl, Guluogou; w, Wuwamen. (c) Simplified geological map of the Central Tianshan (modified from Zhong et al. (2015)).

The North Tianshan is separated from the Yili Block and the Central Tianshan by the North Tianshan Fault and the Main Tianshan Shear Zone, respectively (Figure 1b; Laurent-Charvet et al., 2003). It primarily consists of Late Devonian to Carboniferous sedimentary and volcaniclastic rocks, representing an accretionary complex formed by the southward subduction and accretion of the North Tianshan-Junggar Ocean (Charvet et al., 2011; Han et al., 2010; Ni et al., 2021). The wedge-shaped Yili Block is bordered by the North Tianshan Fault to the north and the Nalati Fault to the south (Figure 1b; Charvet et al., 2011; Wang et al., 2007; Zhong et al., 2017). It mainly comprises Meso-to Neoproterozoic metasedimentary rocks and granitic gneisses, Late Neoproterozoic–Paleozoic sedimentary covers, Paleozoic arc-type igneous rocks, and Permian post-orogenic magmatic rocks

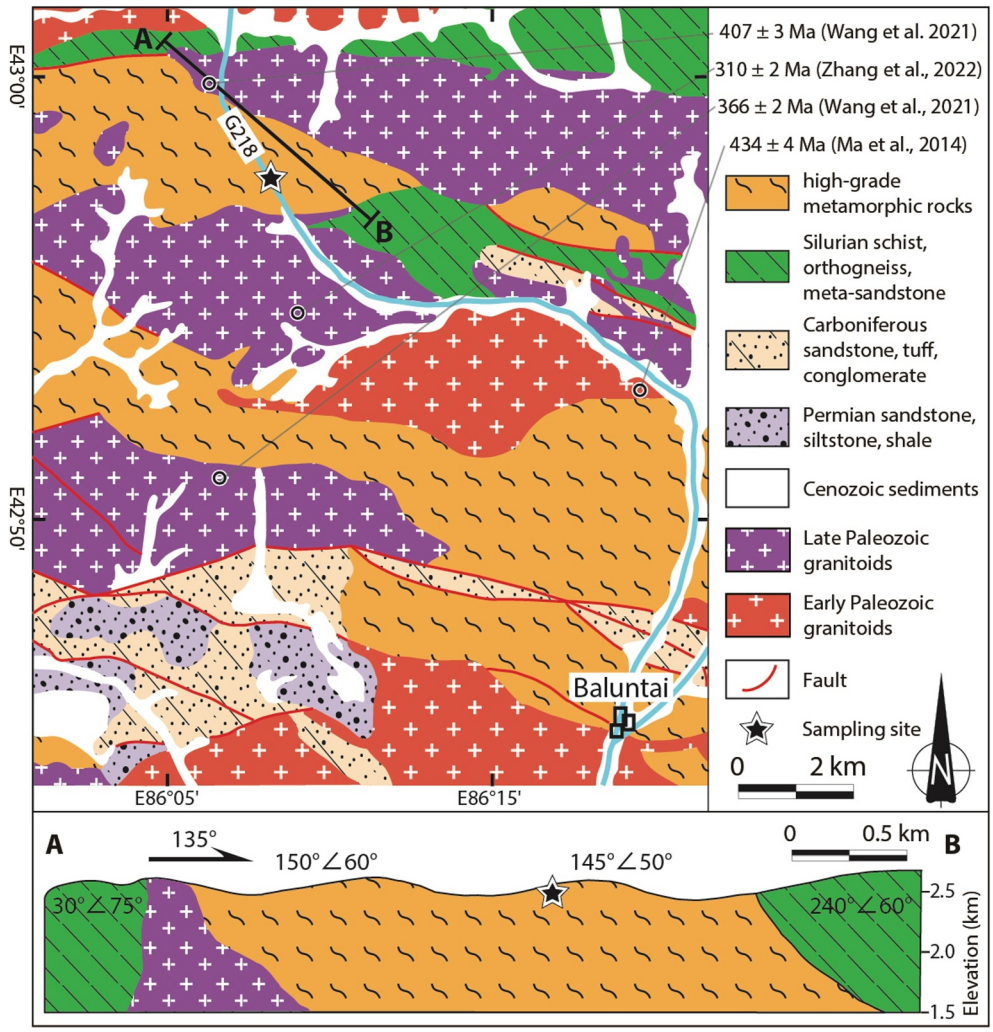

Figure 2. Geological map of the Baluntai area showing Silurian-Permian strata, and the Early Paleozoic and Late Paleozoic plutons (ages are from Ma et al., 2014; Wang et al., 2021; Zhang et al., 2022). The high-grade metamorphic rocks with unclear age are also shown in this map. Section A–B: a cross-section of studied Baluntai migmatites.

(Hu et al., 2010; Liu et al., 2014, 2022; Wang et al., 2014). The South Tianshan refers to the areas bounded by the Nalati Fault and the Baluntai Fault to the north and the South Tianshan ophiolitic mélange zones to the south (Figure 1b; Wang et al., 2018; Zhong et al., 2019). It is chiefly composed of allochthonous units of ophiolites and ophiolitic mélanges and Late Cambrian to Ordovician marine sediments with interlayered volcanic rocks (Han et al., 2011; Jiang et al., 2014; Wang et al., 2011).

The Central Tianshan is a continental block sandwiched between the North Tianshan-Yili Block and South Tianshan; its northern boundary is defined by the Nalati Fault and the Main Tianshan Shear Zone (Gao et al., 1998; Han et al., 2011; He et al., 2018; Wang et al., 2018). However, its southern boundary and westward extent are still controversial (Gao et al., 2011; Han & Zhao, 2018; Zhong et al., 2015). In this study, the Central Tianshan stands only for the Baluntai area, with the Baluntai Fault as its southern boundary. The Central Tianshan contains a Proterozoic crystalline basement composed of Meso-to Neoproterozoic gneiss, amphibolite, mica schist, marble, and minor tillite (Chen et al., 2009; Lei et al., 2011; Shi et al., 2010; XBGMR, 1993). Voluminous Ordovician to Early Devonian subduction-related plutonic rocks are exposed in the Central Tianshan, reflecting a continental arc setting (Dong et al., 2011; Ma et al., 2014; Yang et al., 2006). Ordovician to Silurian sandstones with interlayered volcaniclastic rocks are also outcropped in this region, and they were locally metamorphosed to greenschist facies (Ma et al., 2012; Shu et al., 2011). Late Devonian to Carboniferous undeformed intrusive rocks crosscut the deformed early Paleozoic plutonic rocks and Proterozoic basement and were found to be formed

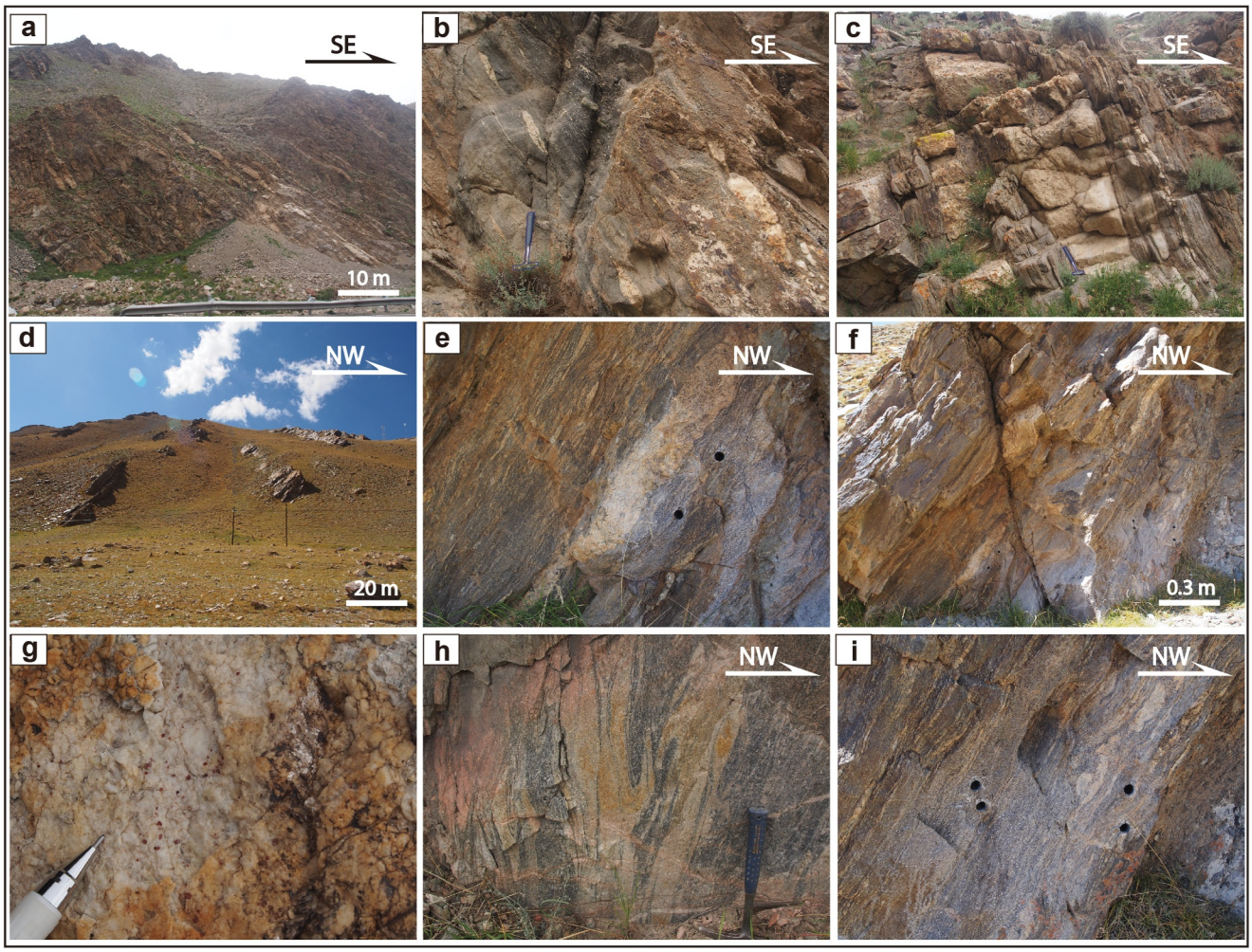

Figure 3. Field photographs of (a, d) migmatites with SE-dip foliation and moderate dip angle; (b, c, e, f) in situ leucosomes as interlayers in melanosomes and mesosomes with widths varying from ~1 cm to several centimeters; lecosome sills of several centimeters to a few meters showing boudinage, rootless lentoid, and wedge-like shapes; (g) leucosomes consisting of quartz, feldspar with minor muscovite and garnet; (h) randomly folded foliations possibly due to syn-migmatitic rheological deformation; (i) felsic minerals occur as tiny lenses or thin layers in stromatic migmatites. The geological hammer (~35 cm in length) and paleomagnetic drill hole (2.2 cm in diameter) serve as scales.

under syn- or post-collisional settings (Ma et al., 2014; Xu et al., 2014; Zhong et al., 2015). Most of the abovementioned rocks are unconformably overlain by the lower Carboniferous molasse of the Maanqiao Formation (Charvet et al., 2007, 2011; Shu et al., 2004; XBGMR, 1993) and the upper sedimentary sequences grading upward into shallow marine carbonates and sandstones (Carroll et al., 1995).

2.2. Field Occurrence of Migmatites in the Baluntai Area and Sampling

High-grade metamorphic rocks including migmatites are widespread in the Central Tianshan (Baluntai area), covering an area of more than 100 square kilometers (XBGMR, 1993; Figures 1c and 2). They were previously assigned as Precambrian rocks, but recent work has found their ages questionable (XBGMR, 1993). Our studied area is located about 25 km northwest of Baluntai town along the national highway G218 (Figure 2). Several granitic plutons exposed nearby with ages ranging from 430 to 310 Ma (Figure 2; Ma et al., 2014; Wang et al., 2021; Zhang et al., 2022). In the studied section, the migmatites generally show consistent foliations with dip directions and dip angles range from 133° to 153°N and 38° to 65°SE, respectively (Figures 2, 3a and 3d). Banded and schlieren migmatites were found to be major lithological variations according to the configuration of leucosomes, melanosomes, and mesosomes in the field (Figure 3).

In situ leucosomes were usually observed as interlayers in melanosomes and mesosomes, with widths varying from ~1 cm to several decimeters (Figure 3). Leucosome sills can also be found parallel to the significant planar structure (compositional layering) with widths of several centimeters to a few meters, showing boudinage, rootless lentoid, and wedge-like shapes (Figures 3a–3c, 3e and 3f). The leucosomes primarily consist of quartz and feldspar with minor muscovite and garnet (Figure 3g). Melanosomes are principally composed of ferromagnesian minerals such as biotite and amphibole, and are developed as restite-rich lenses of centimeter to decimeter-thick layers (Figure 3). The boundaries between melanosomes and mesosomes/leucosomes are obvious, defining the main planar structure in the studied section. Nevertheless, the foliations are sometimes randomly folded, possibly due to syn-migmatitic rheological deformation (Figure 3h). Mesosomes contain both felsic (pale-colored, quartz and feldspar) and restite (darker-colored, biotite and amphibole) minerals. The felsic minerals commonly occur as tiny lenses or thin layers in stromatic migmatites (Figure 3i), hinting at the removal and recrystallization of melt. Speckles of felsic minerals are often developed in massive mesosomes (Figures 3b and 3i), indicating initial formation and recrystallization of melt without apparent segregation and migration from the mesosomes.

A total of 182 standard paleomagnetic cores from 13 sites were collected using a portable drill in the Baluntai area (N42°58′40″–N42°58′55″, E86°06′12″–E86°06′35″). The orientation of core samples was measured by a magnetic compass and a solar compass when possible. The differences between these two azimuths are calculated to be 2.6° ± 3.0° (1σ), indicating the local magnetic declination in the studied region.

3. Methodology

To measure AMS and magnetic remanences, core samples were cut into standard cylindrical paleomagnetic specimens with 2.5 cm in diameter and 2.2 cm in length. The residual samples serve as potential materials to make thin sections and rock powders. Thin sections were produced from leucosomes, melanosomes and mesosomes, and were observed under a microscope to recognize their mineral composition as well as deformation. Unless otherwise specified, the following experiments were carried out in the Paleomagnetism Laboratory of the Institut des Sciences de la Terre d'Orléans (ISTO) at Orleans University.

To constrain the age of migmatization, monazite U-Pb dating was applied because the monazite U-Pb system has the closest closure temperature to the migmatization temperature (Randall, 1990). The monazite dating was performed in situ on two thin sections of migmatites using an electron probe micro-analyzer (EPMA, Cameca SX50) equipped in the ISTO. The electron probe beam is 1 μm in diameter, and the spacing between two analysis points is larger than 5 μm. The analysis paths avoid fractures and inclusions (see Cocherie et al., 1998 for the detailed analysis process). The single point ages were calculated by EPMA dating Excel Macro program file (Pommier et al., 2003), and the weighted average age was obtained in Microsoft Excel.

To estimate the major magnetic minerals in the studied samples, several magnetic experiments were carried out. Rock powders of nine representative samples were used to conduct thermomagnetic experiments utilizing a MFK1 susceptibility meter coupled with a CS-4 furnace in the atmosphere. Magnetic hysteresis loops were determined for these rock powders via a MicroMag Princeton Measurements vibrating sample magnetometer (VSM) equipped in the Paleomagnetic Laboratory of Institut de Physique du Globe de Paris (IPGP). In addition, 10 representative specimens were picked to perform isothermal remanent magnetization (IRM) acquisition experiments utilizing an ASC IM-10-30 impulse magnetizer with maximum applied fields of 1.2 T or 1.5 T.

To study the magnetic fabrics of the migmatites, 145 specimens from 13 sites have been measured via a MFK1 susceptibility meter. The mean orientation of three principal axes of the AMS ellipsoid ($K_1 \geq K_2 \geq K_3$), the anisotropy degree (P_j), and the shape parameter (T) were calculated by the software Anisoft 4.2 (Chadima & Jelínek, 2008). Hoping to estimate the effect of remanence anisotropy on magnetic inclination shallowing of the Baluntai migmatites, we have performed an anisotropy of anhysteretic remanent magnetization (AARM) investigation using an alternating field (AF) demagnetizer coupled with a PARM machine of MOLSPIN LIMITED in the Paleomagnetic Laboratory of Nanjing University. Four representative samples were placed in a 0–95 mT window in the presence of a 0.1 mT direct current (DC) magnetic field to obtain ARM. The ARM was applied in nine different orientations following the procedure of McCabe et al. (1985). The samples were demagnetized using a 100 mT AF field before each position and the remanences were measured using a 2G-755 cryogenic superconducting rock magnetometer.

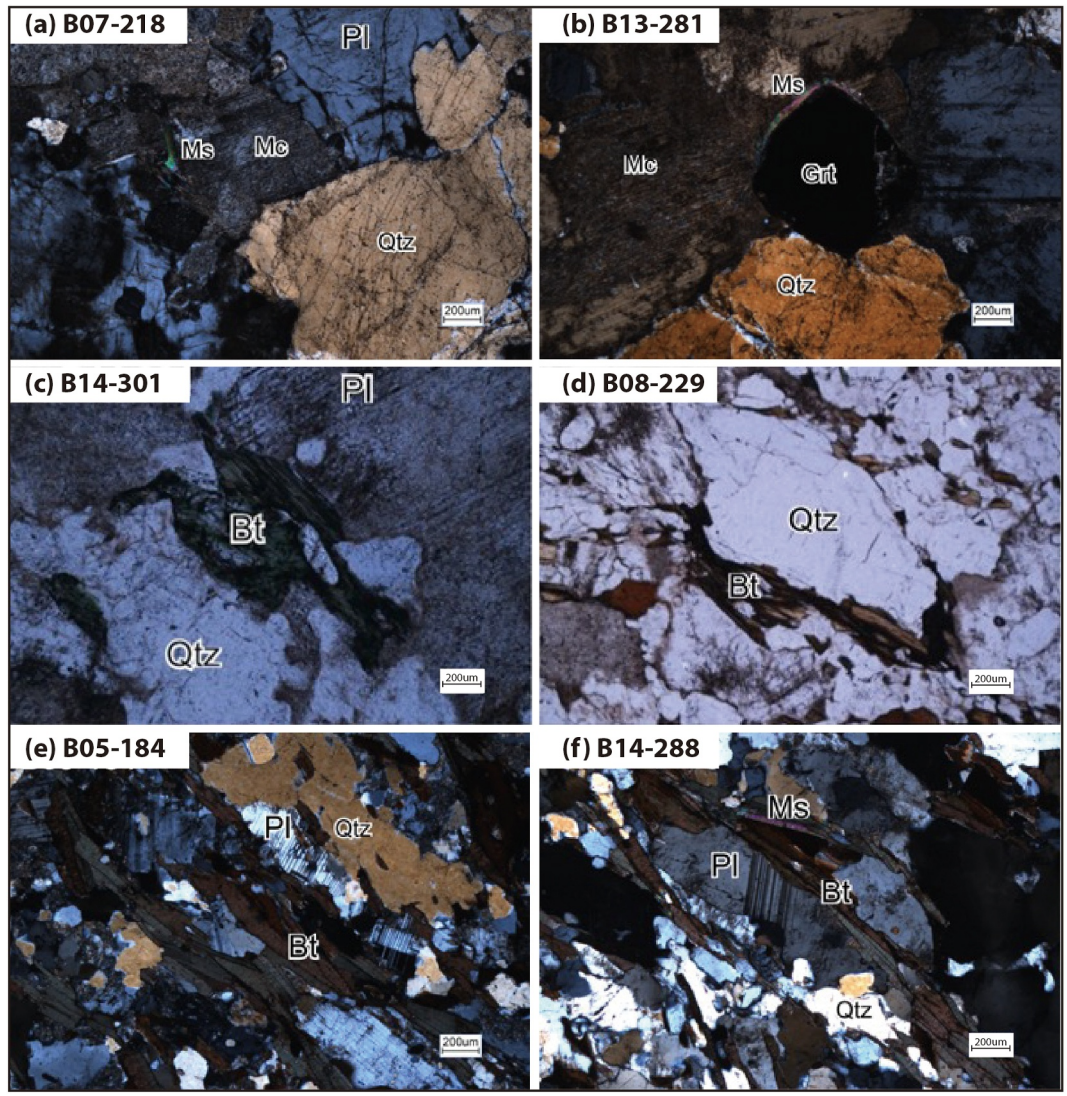

Figure 4. Representative microphotographs of (a, b) leucosomes, (c, d) mesosomes, and (e, f) melanosomes. Abbreviations: Bt, biotite; Grt, garnet; Mcc, microcline; Ms, muscovite; Pl, plagioclase; Qtz, quartz.

Stepwise thermal demagnetization was chosen to isolate the possible characteristic remanent magnetizations (ChRM) of available migmatitic specimens using a laboratory-built furnace. Around 10–14 steps, fewer when the magnetic remanence decreases quickly, were applied with a 50°C increment from room temperature to 500°C and a 20–30°C increment from 500°C to 580°C. The magnetic remanence of specimens was measured with a JR-5A spinner magnetometer. Demagnetization results were plotted on orthogonal vector diagrams (Zijderveld, 1967), and visually identified linear trajectories were used to determine the directions of magnetic components and isolate the ChRM by principal component analysis (Kirschvink, 1980). Mean directions were computed with Fisher spherical statistics (Fisher, 1953). The paleomagnetic data were analyzed with PaleoMac software packages offered by Cogné (2003).

4. Results

The mineral composition and fabric characteristics of different types of migmatites were evaluated through microscopic observations (Figure 4). Concerning the leucosomes, the mineral composition was estimated to be quartz (40%) + plagioclase (30%) + microcline (20%) + garnet (3%) + muscovite (2%) + others; typical magmatic textures were observed (Figures 4a and 4b). The mesosomes are composed of quartz

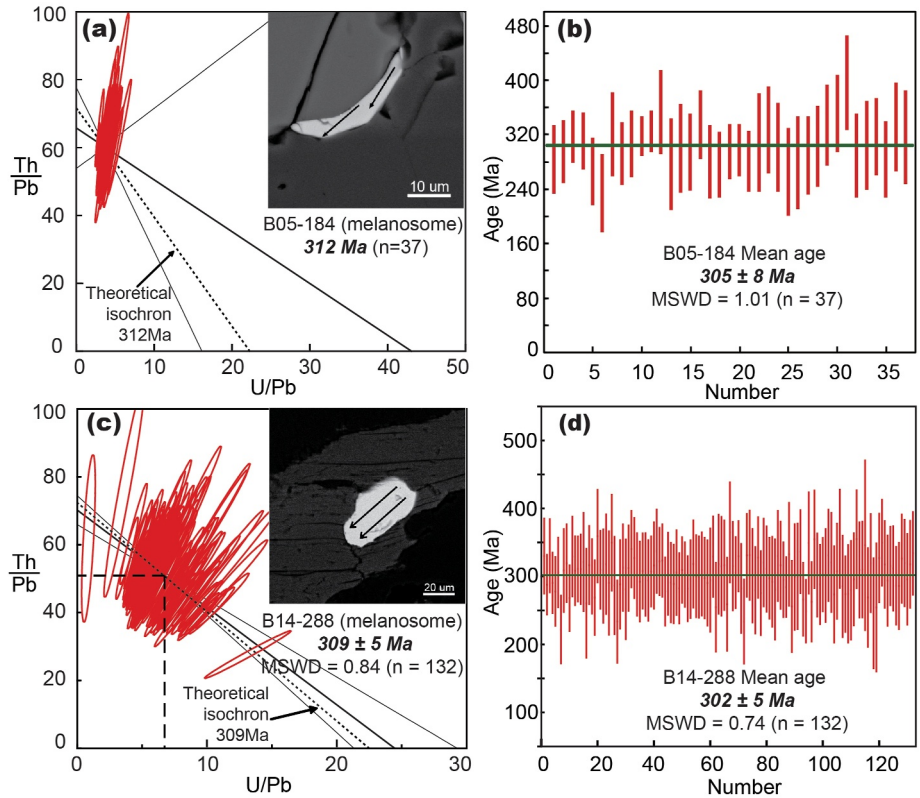

Figure 5. In situ monazite U-Pb dating results of monazites from Samples B05-184 and B14-288. (a, c) Isochron ages; and (b, d) weighted mean ages.

(35%) + plagioclase (40%) + biotite (20%) + muscovite (3%) + others. The quartz and plagioclase occur as porphyroblasts without significant dynamic recrystallization, and the biotite shows a weak shape preferred orientation (SPO; Figures 4c and 4d). The mineral composition of the melanosomes is quartz (20%) + plagioclase (40%) + biotite (35%) + others. The porphyroclasts/blasts of quartz and plagioclase experienced deformation, characterized by the elongation and wavy extinction of fine-grained quartz. Meanwhile, the biotite demonstrates well-defined SPO (Figures 4e and 4f).

4.1. In Situ Monazite U-Pb Dating

Few monazite grains can be found in the leucosomes and their grain sizes are too small to be suitable for dating; therefore, thin sections of two melanosome samples (B05-184 and a B14-288) were selected to perform in situ monazite U-Pb dating. The monazite grains in Sample B05-184 are 20–50 μm in size and mostly subhedral in shape, developing at the boundaries of mineral grains (Figure 5a); 37 dating spots yielded an isochron age of ~312 Ma (Figure 5a) and a mean age of 305 ± 8 Ma (MSWD = 1.01; Figure 5b). In addition, the monazite grains in Sample B14-288 are larger (50–100 μm) with euhedral shapes and usually grow inside biotites (Figure 5c); 132 dating spots provided an isochron age of 309 ± 5 Ma (MSWD = 0.84; Figure 5c) and a mean age of 302 ± 5 Ma (MSWD = 0.74; Figure 5d). In conclusion, all these ages are consistent considering the uncertainties, indicating that the cooling age of monazites in the studied migmatites is ~314–297 Ma. Detailed data can be found in Table S1.

4.2. Rock Magnetic Analyses

The hysteresis loops of leucosomes generally show low magnetic moment with a small nonlinear component between ±200 mT. With the applied magnetic field increasing, the magnetic moments of leucosomes increase or decrease linearly (Figure 6a), suggesting that the leucosomes are mainly composed of diamagnetic minerals (quartz and feldspar) with a variable amount of paramagnetic minerals (biotite) and perhaps a few ferromagnetic

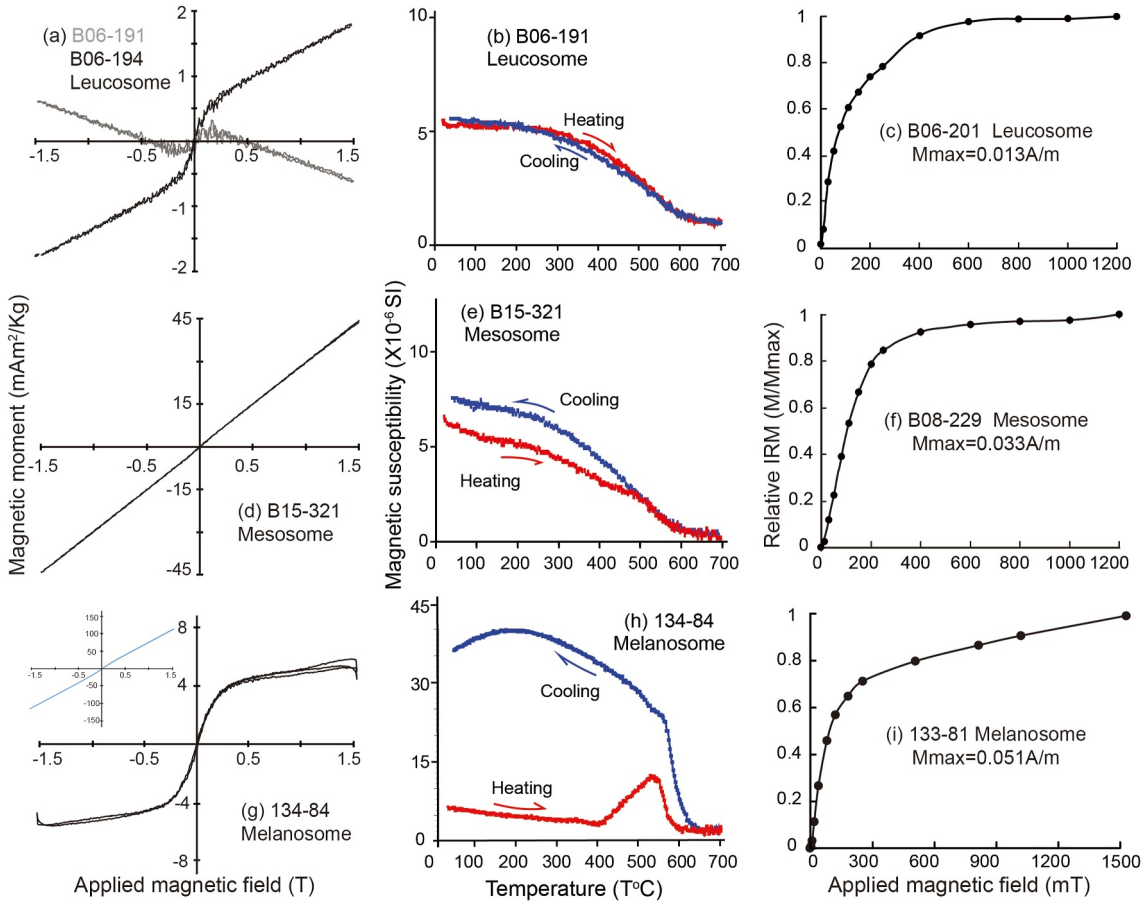

Figure 6. Hysteresis loops (a, d, g), thermomagnetic curves (b, e, h), and isothermal remanent magnetization acquisition curves (c, f, i) of representative samples from leucosomes, mesosomes, and melanosomes, respectively.

minerals. The thermomagnetic curves of leucosomes show an evident decrease in magnetic susceptibility from ~300°C to ~600°C during heating and are reversible during cooling (Figure 6b), indicating the existence of titanomagnetite and the absence/weakness of mineralogical transformation. The IRM acquisition curves present a rapid increase of IRM below 200 mT and a relatively slow increase from 200 to 600 mT (Figure 6c), implying the possible coexistence of titanomagnetite with some high coercivity minerals. The hysteresis loops of the mesosomes are linear with positive slopes (Figure 6d), indicating the dominance of paramagnetic minerals (i.e., biotite). Minor ferromagnetic minerals with low coercivity (i.e., titanomagnetite) are also supposed to be contained in the mesosomes based on the fact that the magnetic susceptibility shows significant decreases during heating at ~200–600°C (Figure 6e), and the IRM increases rapidly below 200 mT (Figure 6f). Much more paramagnetic minerals (i.e., biotite) are suggested to exist in the melanosomes because the magnetic moment is about three times larger than that of the mesosomes at a given applied magnetic field (Figures 6d and 6g) and the IRM increases with a constant slope over ~200 mT (Figure 6i). A few low-coercivity ferromagnetic minerals (e.g., titanomagnetite) also exist in the melanosomes in the light of the thermomagnetic curves and a rapid increase of IRM below 200 mT (Figures 6h and 6i).

4.3. Magnetic Fabrics

The mean magnetic susceptibility [$K_m = (K_1 + K_2 + K_3)/3$] of the migmatite samples varies from -4×10^{-6} [SI] to 790×10^{-6} [SI]; 143 out of 145 studied samples have K_m values smaller than 354×10^{-6} [SI] with an average value of 111×10^{-6} [SI] (Figure 7a). 130 out of 145 samples show P_j values below 1.50, ranging between 1.02 and 1.49 with an average of 1.20 (Figure 7b); the P_j values of the remaining 15 samples, mostly being melanosomes, vary from 1.51 to 2.10 with an average value of 1.83 (Figure 7b). The shape parameter T of migmatite samples ranges between −0.72 and 0.99 with an average of 0.64, showing an oblate shape dominance (~95%; Figure 7c).

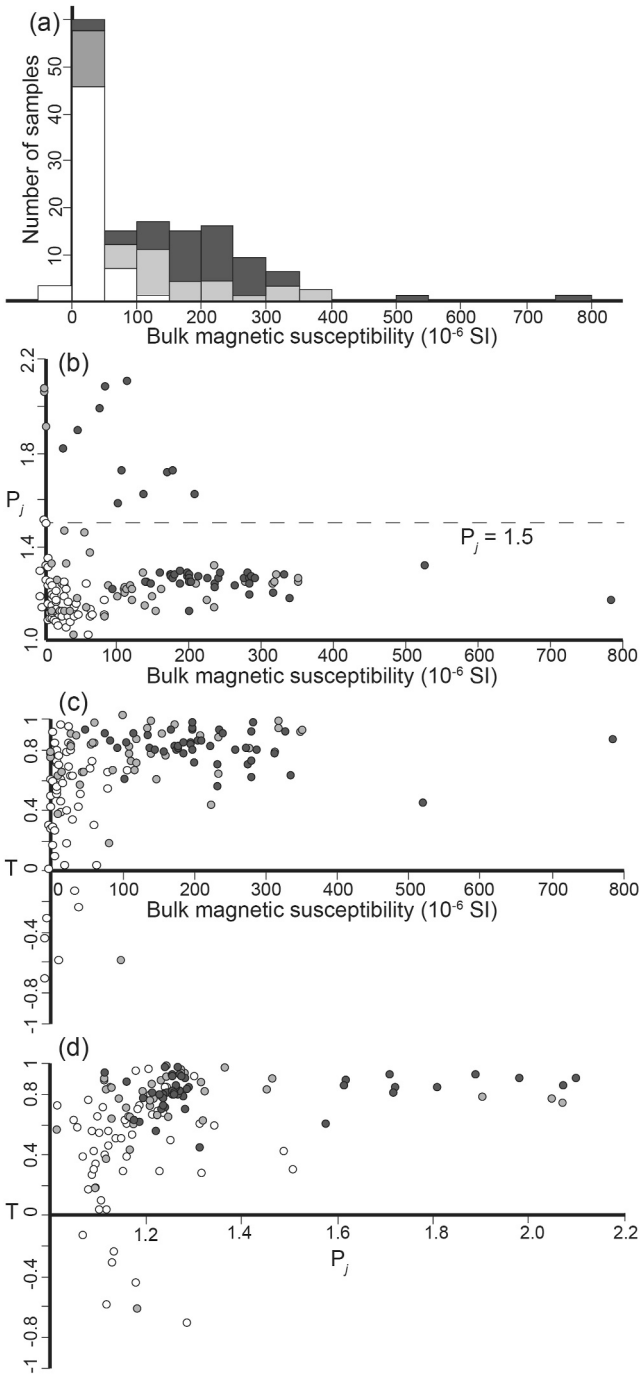

Figure 7. AMS scalar parameters of the Baluntai migmatites: (a) histogram of bulk magnetic susceptibility (Km) of samples; (b) anisotropy degree P_j value versus bulk magnetic susceptibility Km; (c) shape parameter T versus bulk magnetic susceptibility Km; (d) shape parameter T versus anisotropy degree P_j value. White, light-gray, and dark-gray symbols represent leucosomes, mesosomes, and melanosomes, respectively.

No significant correlation between K_m, P_j, and T is observed, indicating that AMS varies independently from the magnetic minerals (Borradaile & Henry, 1997; Figures 7b–7d). Detailed AMS data are shown in Table S2.

Specifically, the leucosomes have K_m values between -4×10^{-6} [SI] and 113×10^{-6} [SI] with an average K_m of 26×10^{-6} [SI], P_j values between 1.02 and 1.51 with an average of 1.15, T values from −0.72 to 0.96 with a dominance of oblate shape (~89%) and an average of 0.43. The mesosomes show K_m values between 1×10^{-6} [SI] to 354×10^{-6} [SI] with an average of 130×10^{-6} [SI], P_j values between 1.02 and 2.07 with an average of 1.28, T values from −0.63 to 0.98 dominated by oblate shape (~98%) with an average of 0.73. The melanosomes possess K_m values between 28×10^{-6} [SI] to 790×10^{-6} [SI] with an average K_m value being 220×10^{-6} [SI], P_j values between 1.12 and 2.10 with an average of 1.38, T value from 0.44 to 0.98 with an average of 0.81.

Although the K_m values of the Baluntai migmatites are generally low, the magnetic parameters were calculated for two samples (Mrs/Ms = 0.01 and 0.02, magnetic remanence/saturation remanence; Hcr/Hc = 6.5 and 5.4, remanent coercivity/coercivity) suggesting that the grain size of the magnetites of the Baluntai migmatites is not within the single domain (Dunlop, 2002). Hence, the principal axes of the magnetic susceptibility ellipsoid correspond to the major morphological axes of constituent minerals. The magnetic fabrics show similar and straightforward patterns for different types of Baluntai migmatite (Figures 8a–8d). Overall, the in-situ maximum axis K_1 and intermediate axis K_2 of the migmatites constitute a girdle representing the magnetic foliation with a dip direction of 177.9° ± 61.5° and a moderate dip angle of 52.9° ± 15.2° (Figure 8a), which is consistent with the foliations observed in the field within the uncertainty (Figure 3). After tilt correction using the attitude of foliations, the K_3 axes of migmatites clusters to be perpendicular to the horizontal plane with vertical inclination (87.9° ± 13.0°), while the K_1 and K_2 axes scatter horizontally (Figure 8a).

The principal axes of the magnetic remanence anisotropy ellipsoid have been calculated according to Girdler (1961). The remanence anisotropy degrees of the studied samples range from 1.51 to 1.86, significantly higher than their susceptibility anisotropy degrees varying from 1.26 to 1.33 (Table S3).

4.4. Paleomagnetism

About 160 migmatite samples were thermally demagnetized, three-fourths of which, unfortunately, show erratic demagnetization trajectories and cannot be used for further analysis (e.g., Figure 9a). The lack or low content of ferromagnetic minerals, as evidenced by the rock magnetic analyses and low K_m values (Figures 6 and 7a), could be the main reason for such unstable demagnetization results. The majority of meaningful demagnetization diagrams generally display two magnetic components, a low-temperature component (LTC) and a high-temperature component (HTC). A total of 29 samples present a LTC below 200–250°C with an in-situ mean direction of D_g = 4.6°, I_g = 59.9° (k_g = 13.7, a_{95g} = 7.5°), which is insignificantly different from the present-day geomagnetic field (IGRF: D = 3.0°, I = 63.4°) in the Baluntai area (Figures 9b, 9c and 10a; Table S4). The precision parameter (k) slightly decreases from 13.7 to 13.3 after correction using the attitude of foliation, suggesting an inconclusive fold test mainly due to the monoclinal foliation of studied migmatites (Figure 10b). The HTC can generally be isolated at temperatures of 200–300°C to 400–580°C and decay linearly to the origin (Figures 9d–9i; Table S4). The Fisher mean of in-situ HTC directions is calculated as D_g = 230.7°, I_g = −25.2° (k_g = 24.8,

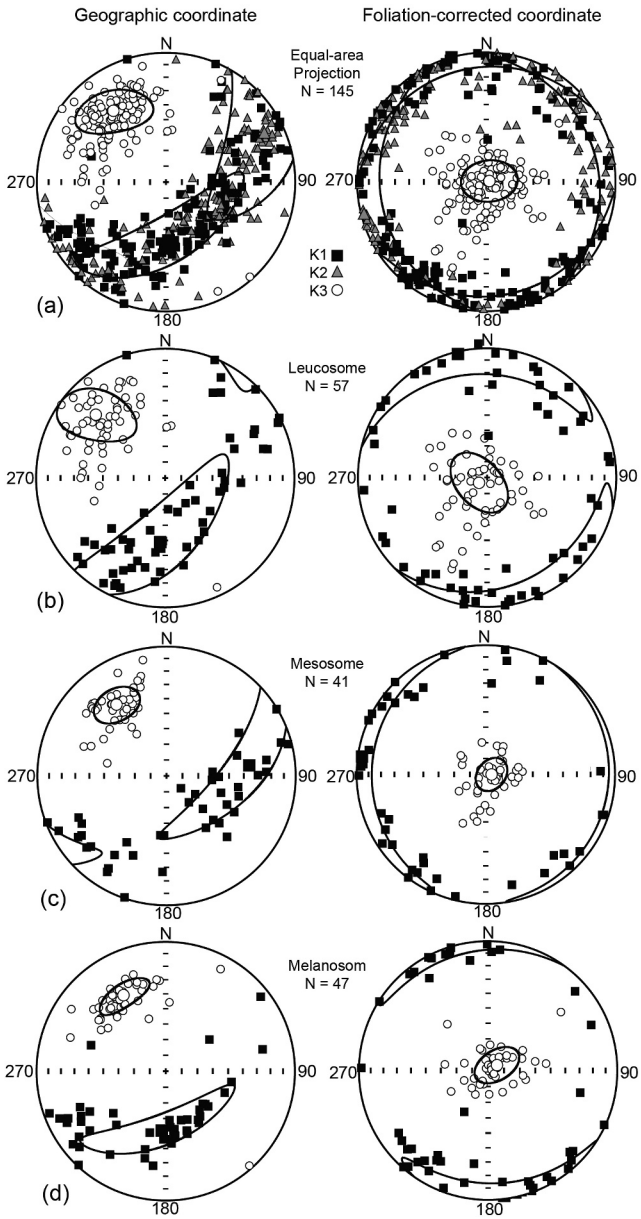

Figure 8. Anisotropy of magnetic susceptibility analyses results for (a) all samples, (b) leucosomes, (c) mesosomes, and (d) melanosomes, respectively, in geographic and foliation-corrected coordinates.

a_{95g} = 4.5°, n = 43; Figure 10c; Table S4) and a foliation-corrected Fisher mean direction is estimated at D_c = 254.7°, I_c = −15.1° (k_c = 18.8, a_{95c} = 5.2°, n = 43; Figure 10d; Table S4). As the foliations of the studied migmatites are generally monoclinal, no meaningful fold test could be obtained (McElhinny, 1964; McFadden & McElhinny, 1990).

5. Discussion

5.1. Acquisition Mechanism of the Magnetic Fabric of the Baluntai Migmatites

Magnetic fabrics have long been regarded as proxies for mineral fabrics in different materials (e.g., Hrouda, 1982; Rochette et al., 1992; Tarling & Hrouda, 1993) and were suggested to be valuable for studying petrofabrics of migmatites (e.g., Ferré et al., 2003; Kruckenberg et al., 2010). Nevertheless, the kinematic significance of magnetic fabrics may be questioned due to the presence of ferromagnetic minerals that dominate the magnetic properties and generally account for only a minor volume of rocks. Considering that the subfabrics carried by ferromagnetic and paramagnetic minerals could have formed at different stages and experienced distinct deformation paths, separating different subfabrics is an essential issue for interpreting magnetic fabrics (Ferré et al., 2004).

The magnitude of the bulk magnetic susceptibility (K_m) is the sum of diamagnetic (K_{dia}), paramagnetic (K_{para}), and ferromagnetic (K_{ferro}) susceptibility contributions, that is, $K_m = C_{dia}\cdot K_{dia} + C_{para}\cdot K_{para} + C_{ferro}\cdot K_{ferro}$, where C_{dia}, C_{para}, and C_{ferro} are the respective concentrations. In general, the diamagnetic contribution is relatively weak compared to the two others, and it could be estimated by the content of diamagnetic minerals. In our case, the diamagnetic minerals in the migmatites are quartz and feldspar accounting for 60%–90% volume of the rock. Since the intrinsic magnetic susceptibility of these minerals is indicated to be around -14×10^{-6} [SI] (e.g., Borradaile et al., 1987), the calculated diamagnetic contribution to K_m is around -10×10^{-6} [SI]. As for the paramagnetic contribution, its maximum theoretical value (K_{para*}) could be calculated using the formula of Syono (1960) and Rochette (1987): $K_{para*} = -14.6 + \rho/1{,}000 \times [25.2 \times Fe^{2+} + 33.4 \times Fe^{3+} + 25.2 \times Mn^{2+}] \times 10^{-6}$ [SI], where ρ is the rock density and Fe^{2+}, Fe^{3+}, Mn^{2+} are the atomic weight percentages. A mean density of ∼2,750 kg/m^3 of migmatites (Saxov & Abrahamsen, 1964; Southwick & Chandler, 1996) and the chemical composition of comparable Naxos migmatites and Morton granite gneisses (Pe-Pier et al., 1997; Wooden et al., 1980) were used to calculate a K_{para*} value that is around (175–306) × 10^{-6} [SI]. Out of 145 studied samples, only ten (∼7%) have K_m values larger than 306 × 10^{-6} [SI], indicating that most of the Baluntai migmatites are essentially paramagnetic (Figure 7a). Moreover, according to the formula $K_{ferro} = K_m - K_{para} - K_{dia}$, it could be concluded that the ferromagnetic contribution to the K_m of most migmatites is negligible. Therefore, the magnetic fabrics of the Baluntai migmatites are dominated by paramagnetic minerals and could be safely correlated with petrofabrics.

Biotite is the most abundant paramagnetic mineral in the Baluntai migmatites, which defines macroscopic foliations widely observed in the field. Hereby, the magnetic fabrics of the Baluntai migmatites originate from the lattice-preferred orientation of biotite (LPO; magnetocrystalline anisotropy) which is generally similar to the SPO. Previous electron backscatter diffraction studies on biotite suggest a strong correspondence between K_3 (as well as the pole to macroscopic foliation) and the <001> direction of biotite; meanwhile, the magnetic lineation K_1 of migmatites is indicated to arise from biotite crystals that have a zone axis orientation about the viscoplastic flow direction (e.g., Borradaile & Werner, 1994; Kruckenberg et al., 2010). For the Baluntai migmatites, no

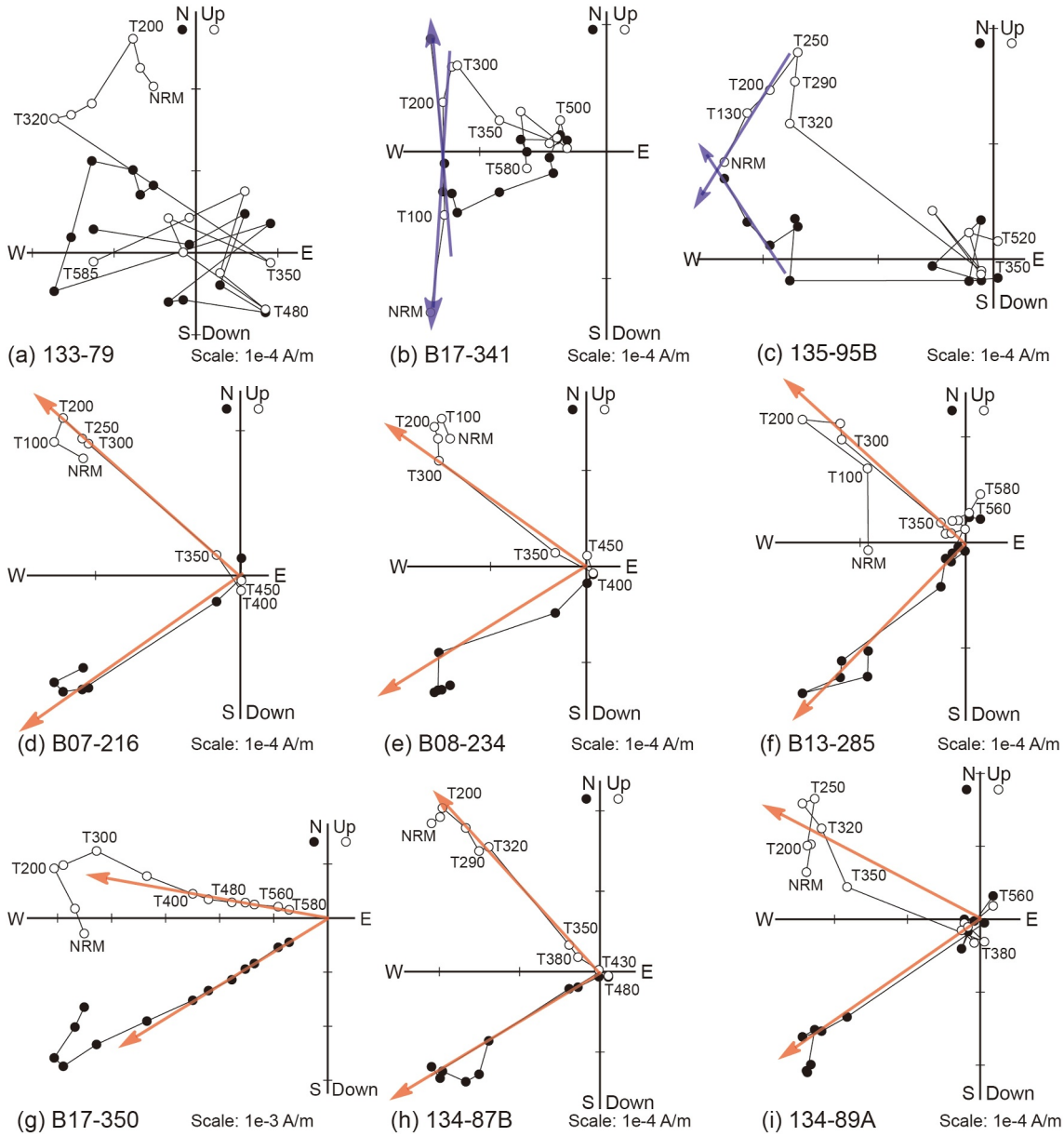

Figure 9. Representative demagnetization curves in the geographic coordinates for samples from the Baluntai migmatites. Note: blue arrows stand for low unblocking temperature component (LTC) and red arrows represent characteristic remanent magnetization (ChRM).

clustered magnetic lineation K_1 in either geographic coordinates or after foliation correction suggests the absence of an evident preferred viscoplastic flow (Figure 8). In contrast, a vertical K_3 axis (87.9° ± 13.0°) was determined clearly after foliation correction (Figure 8). Furthermore, different types of migmatites present identical magnetic fabrics with some differences in magnetic parameters (Figures 8b–8d). Notably, the anisotropy degree P_j increases from leucosomes, mesosomes to melanosomes (average values from 1.15, and 1.28 to 1.38, respectively; Figure 7b). This phenomenon probably results from the partial melting and segregation process because the P_j values of quartz and feldspar are weak compared to that of biotite that could reach to a maximum value of 1.23–1.50 with a mean value of 1.36 (Biedermann et al., 2016; Borradaile & Werner, 1994; Zapletal, 1990).

Foliation of metamorphic rocks is formed by differential stress. In the Baluntai migmatites, biotites would rotate or grow in a differential stress regime to have their individual minimum axes perpendicular to the foliation that their alignment creates. On average, the temperature increases by about 25°C for every kilometer of depth (Wolfson, 2012). Considering that the Baluntai migmatites are high-grade metamorphic rocks formed at ~500–

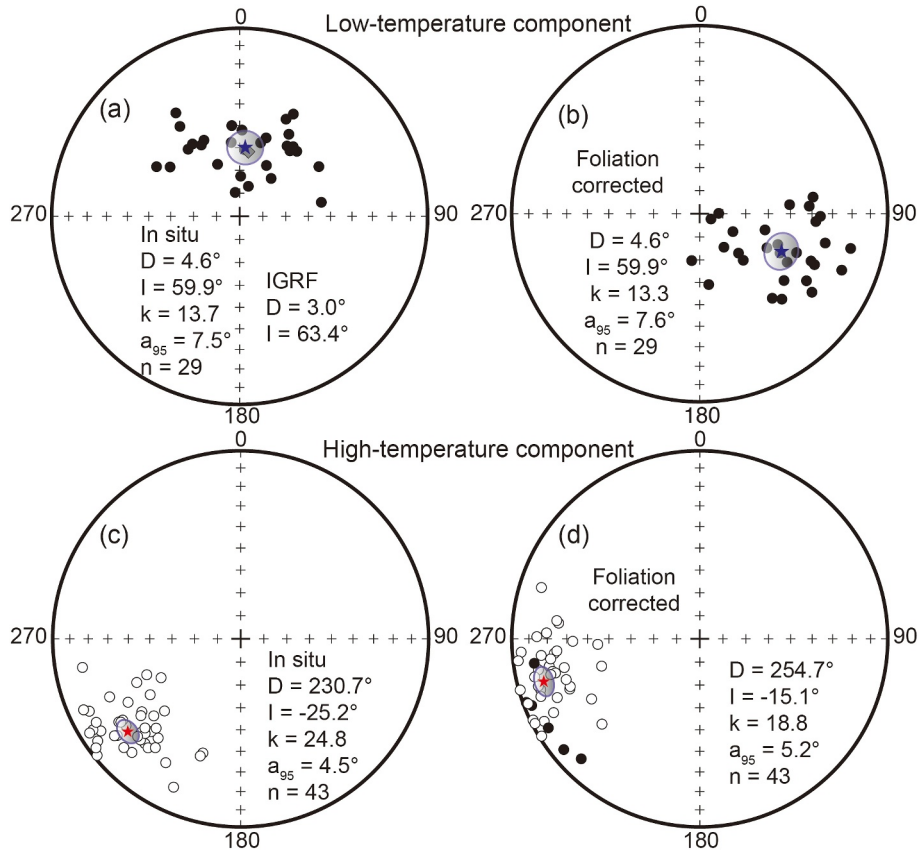

Figure 10. Equal-area projections of isolated LTCs and ChRMs in the geographic coordinates (a, c) and the foliation-corrected coordinates (b, d), respectively. International Geomagnetic Reference Field (IGRF, gray quadrangle) is shown in (a) as a reference.

600°C, their buried depth can be estimated as ∼20–24 km. Applying an average crustal density of 2,775 kg/m^3 in orogens (Artemieva & Shulgin, 2019), the lithostatic pressure of the Baluntai migmatites was found to be ∼540–650 Mpa. On the other hand, as the Baluntai migmatites were formed in an orogenic environment, the horizontal tectonic stress should be significant. Extensive previous research has been conducted to estimate the magnitude of differential stress within the Earth's crust. It can be evaluated utilizing heat flow or seismological data (e.g., Brune et al., 1969; Molnar & England, 1990; 1–100 Mpa), predicted by extrapolation of experimental data on rock strength (e.g., Hanks, 1977; 20–100 Mpa), deduced from tensile fracturing directly relevant to orogenic processes (Etheridge, 1983; 20–40 Mpa), or measured directly in the uppermost part of the lithosphere (e.g., Fialko et al., 2005; McGarr & Gay, 1978; several 10s Mpa). Alternatively, the magnitude of differential stress can be derived from the microstructures in exhumed rocks (e.g., Twiss, 1977). However, the calibrations of these paleopiezometers are with significant uncertainty (Poirier, 1985). At this stage, we can make a comparison between the tectonic stress and lithostatic pressure of the Baluntai migmatite. Taking a maximum value of 100 Mpa for the tectonic stress and a minimum value of 540 Mpa for lithostatic pressure, the maximum dip angle of the intermediate-minimum stress plane can be calculated with arctan (100/540), that is, ∼10°, which is within the uncertainty of the AMS data (Figure 8). Therefore, the maximum stress axis of the differential stress of the Baluntai migmatites was closer to vertical and the foliation was probably originally formed in a horizontal geometry. In addition, the foliations of the Baluntai migmatites and the contacted Silurian schists are distinct (Figure 2; XBGMR, 1993).

Consequently, the acquisition mechanism of the magnetic fabrics of the Baluntai migmatites could be put forward as below: (a) the protoliths of migmatites experienced significant deformation dominantly due to lithostatic pressure, showing intermediate P_j and T values as suggested by mesosomes (Figures 11a and 11d); (b) with partial melting occurred, quartzo-feldspathic materials started to melt, while ferromagnesian minerals like biotite are

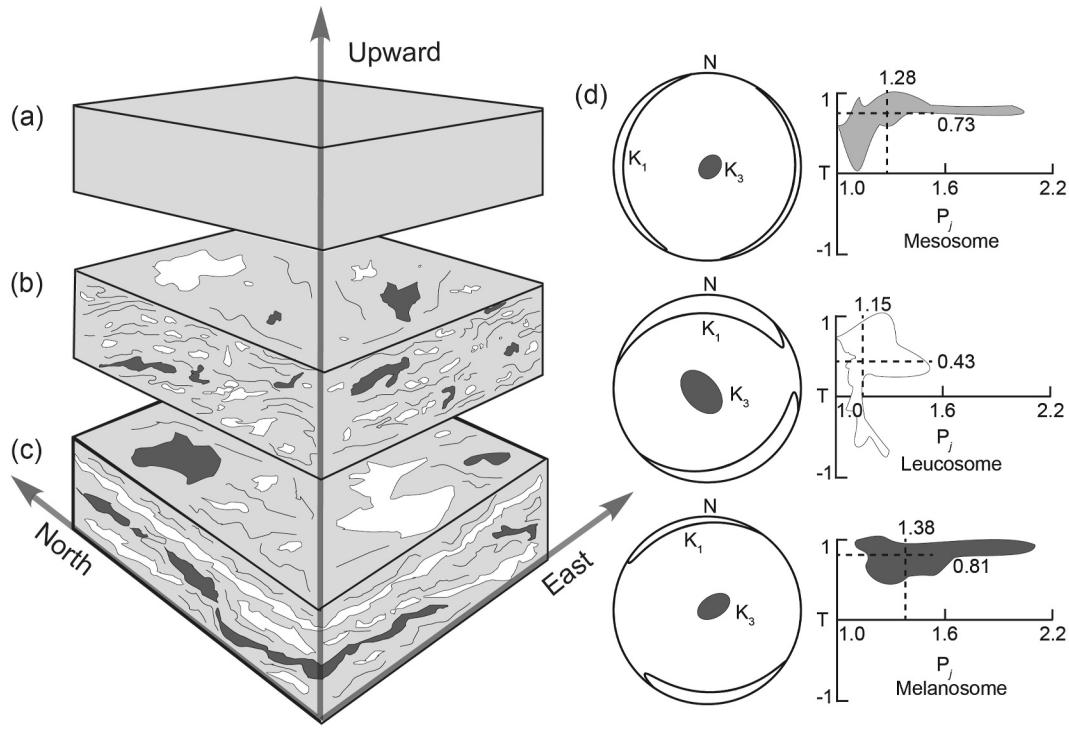

Figure 11. Cartoon schematic diagram showing the acquisition process of the magnetic fabrics in the Baluntai migmatites from (a) protoliths to (b) initial migmatites to (c) mature migmatites; (d) schematic diagram of AMS results and T-P_j plots with mean values for different elements of migmatites. The white, light-gray, and dark-gray symbols indicate leucosomes, mesosomes, and melanosomes, respectively.

refractory and left autochthonous (Figure 11b); (c) as the quartzo-feldspathic materials accumulated, they tended to segregate from the protolith and form leucosomes with low P_j and T values; in contrast, the residual became melanosomes with high P_j and T values (Figures 11c and 11d). Since the abovementioned types carry essentially identical petrofabrics (Figure 11d), they should have formed under a stable paleostress field.

5.2. Interpretation of the Paleomagnetic Results From the Baluntai Migmatites

In view of the K_m of the Baluntai migmatites, their content of ferromagnetic minerals is generally minor (Figure 7a). Our demagnetization results prove this conclusion. Three-fourths of samples show erratic demagnetization behaviors with low remanent magnetization of 10^{-4} A/m level (Figure 9), which is several orders lower than that of common paleomagnetic targets (e.g., redbeds/volcanic rocks and mafic dikes; Zhu et al., 2019, 2023). However, meaningful LTC and HTC components were successfully isolated from 29 to 43 samples, respectively (Figures 9 and 10). The LTC component is probably a recent viscous overprint since it is indistinguishable from the present-day geomagnetic field (Figure 10a). In contrast, the origin and implication of the HTC component are less evident and need careful consideration.

In-situ monazite U-Pb dating results suggest a cooling age of ~314–297 Ma for the Baluntai migmatites (Figure 4), hinting that the magnetic remanence carried by the migmatites should not be older than ~314 Ma. Furthermore, a muscovite $^{40}Ar/^{39}Ar$ plateau age of a migmatitic granite and a biotite $^{40}Ar/^{39}Ar$ plateau age of a melanosome in the Baluntai area were found to be 311 ± 7 and 311 ± 8 Ma, respectively (Zhu, 2020). These geochronological data indicate a cooling history of the Baluntai migmatites at ~314–303 Ma, which likely corresponds to an exhumation event. In summary, the magnetic remanences carried by the Baluntai migmatites should have been acquired during this cooling process in the latest Carboniferous (~314–303 Ma).

Before interpreting our new data, the published Carboniferous paleomagnetic results from the adjacent Tarim and Yili blocks are briefly summarized here to constrain the paleolatitude of the Central Tianshan. For the Tarim Block, at least four Carboniferous paleomagnetic poles have been published, both of which are preliminary results

derived from limestones and sandstones (e.g., the Kangkelin Formation; Bai et al., 1987; Fang et al., 1996; Meng, 1991; Zhai et al., 1988). Some results pass the fold and baked-contact test (e.g., Fang et al., 1996), and the paleolatitudes of the Tarim Block estimated from these poles are consistent at 24–33°N. Concerning the Yili block, no pre-Late Carboniferous paleomagnetic pole has been reported due to the pervasive remagnetization (Wang et al., 2007). The only Late Carboniferous results were reported from tuffaceous sandstones, basalts, and red sandstones in the Zhaosu, Xinyuan, and Gongliu areas (Wang et al., 2007). This study suggests a paleolatitude of 24 ± 6°N for the Yili Block in the Late Carboniferous. Despite the different viewpoints on the relative paleogeography of the paleo-Tianshan Ocean (South Tianshan Ocean) and the Central Tianshan during the Late Paleozoic (e.g., Charvet et al., 2007; Gao et al., 1995; Han & Zhao, 2018; Wang et al., 2018; Xiao et al., 2013), there is a consensus on the paleolatitudinal relationship between the Tarim, Central Tianshan, and Yili blocks. Therefore, the paleolatitude of the Central Tianshan (i.e., Baluntai area) can be estimated as ∼24–30°N in the Late Carboniferous.

According to the above estimation, the paleomagnetic inclination of the Central Tianshan in the Late Carboniferous should range from −42° to −49° (reference site: 43.0°N, 86.1°E). However, the paleomagnetic inclination obtained from our study is much shallower than the expected one both in geographic ($I_g = -25.2°$, $a_{95g} = 4.5°$) and foliation-corrected coordinates ($I_c = -15.1°$, $a_{95c} = 5.2°$). Because the migmatites are foliated (Figure 3), the ChRMs may be deflected to the AMS foliation plane (K_1–K_2 plane) due to magnetic anisotropy (D'Agrella-Filho et al., 2004; Raposo et al., 2003). A correction of the effect of magnetic anisotropy on ChRM directions was performed on high-grade metamorphic rocks from the Juiz de Fora Complex (Raposo et al., 2003), in the light of which the angular difference between deflected ChRM and corrected one is positively correlated with the degree of susceptibility anisotropy. For the samples with degrees of susceptibility anisotropy smaller than 1.8 and 1.5, the angular differences are generally smaller than 10° and 5°, respectively (see Table 1 in Raposo et al., 2003). In our case, 130 of 145 Baluntai migmatite samples provide P_j values below 1.50, and the P_j values of the rest 15 samples show an average of 1.83 (Figure 7b). Our AARM investigation indicates that the remanence anisotropy degree of the Baluntai migmatites is significantly higher than their susceptibility anisotropy degree, suggesting an important contribution of the remanence anisotropy to the abnormal shallow inclination (Table S3). Although our investigation is preliminary due to the lack of a coercivity spectra analysis and the limited sample number, we applied a grain anisotropy of 4/3 in the flattening factor equation of Jackson et al. (1991) to estimate the effect of magnetic anisotropy on magnetic inclination shallowing (Kodama, 1997; Li & Kodama, 2016). Unfortunately, no meaningful flattening factor could be obtained probably due to the strong anisotropy.

Keeping the important effect of remanence anisotropy in mind, three possibilities could also be carried out to interpret the abovementioned anomalous paleomagnetic inclination: (a) an unrepresentative record of the Late Carboniferous paleomagnetic field due to a spot recording, that is, the paleosecular variation is not averaged out; (b) the paleomagnetic results from the Baluntai migmatite have undergone post-Carboniferous remagnetization and cannot be used to estimate the latest Carboniferous paleolatitude of the Central Tianshan; (c) a latest Carboniferous magnetization (during diagenetic cooling related to exhumation) or remagnetization (during posterior thermal disturbance) occurred on the migmatites after the acquisition of magnetic fabrics, and the foliation is invalid in restoring the paleohorizontal.

Concerning possibility A, because the A_{95} of the isolated ChRMs is within the N-dependence A_{95} envelope proposed by Deenen et al. (2011) (A_{95min}, A_{95max} = 2.67, 7.67, A_{95} = 3.82 and 4.10 in geographic and tectonic coordinates, respectively), the PSV appears to have been averaged out. This is supported by the angular dispersion of the corresponding VGPs (S = 14.1° and 15.1° in geographic and tectonic coordinates, respectively) which is similar to the dispersion of S = 15.6° [14.0°, 16.9°] found in VGP populations from 0 to 5 Ma lavas at 44.8°N (Johnson et al., 2008). As for possibility B, no field test is available to determine whether the isolated ChRMs are primary, but a post-Carboniferous remagnetization is unlikely because neither intense magmatism nor strong metamorphism occurred in the Baluntai area after the Carboniferous and contemporaneous primary magnetic remanences have been reported in the neighboring areas (Carroll et al., 1995; Charvet et al., 2007, 2011; Fang et al., 1996; Shu et al., 2004; Wang et al., 2007; XBGMR, 1993). Scenario C seems the most probable. Abundant strike-slip movements were reported in and around the Central Tianshan at the end Carboniferous, such as the sinistral Wulasitai shearing (∼312–301 Ma) and dextral Xiaergou shearing (∼312–295 Ma) as well as the dextral Main Tianshan Shear Zone and Baluntai fault (He et al., 2021; Li et al., 2017; P. F. Li et al., 2020; Wang et al., 2008; Yin & Nie, 1996; Zhu et al., 2018). These transcurrent tectonics could be responsible for the latest Carboniferous remagnetization of the Baluntai migmatites, or even their formation and exhumation (and thus

magnetization). At this stage, we cannot distinguish between these two possibilities because the comparison is unknown between the ambient temperature of Baluntai migmatites and the Curie temperature of main magnetic minerals when the transcurrent tectonics was operating, which is principally determined by the buried depth of the Baluntai migmatites at that time. The foliation of Baluntai migmatites that was formed during the migmatization process cannot be used to restore the paleohorizontal where the isolated magnetic remanences were acquired. We acknowledge that due to the unknown paleo-plane, the posterior tilting of the migmatites after obtaining magnetic remanences could be complicated. Nevertheless, based on Occam's razor, to interpret the anomalous shallow magnetic inclination, a ∼10°–20°SW-down tilting would be the simplest and most likely way to reach the present geometry. This is not without reason, because the regional tectonic planes (e.g., ductile and brittle faults) have NW–SE strikes, and the regional paleostress during the Meso-Cenozoic were N–S originated from the far-field effect of collision events in the Tethyan domain (Figure 1c; e.g., Wu et al., 2020).

5.3. Do Primary Magnetic Fabrics Imply Primary Magnetic Remanences?

Titanomagnetite appears to be the main magnetic remanence carrier of the Baluntai migmatites based on the rock magnetic investigations and demagnetization behaviors (Figures 6 and 9). Within the titanomagnetite series ($Fe_{3-x}Ti_xO_4$), the Ti^{4+} cations enter the inverse spinel structure of magnetite (Fe_3O_4) and substitute for Fe^{3+} as Ti content increases. There are negative dependences of saturation magnetization and Curie temperature upon Ti content for the titanomagnetite series (Nagata, 1961). In the Baluntai case, most measured samples are fully demagnetized at temperature between 400 and 430°C (Figure 9), likely corresponding to titanomagnetites with a Ti content (x) of ∼0.2 (an average approximation; Nagata, 1961). When the ambient temperature surpasses the Curie temperature, the titanomagnetites become paramagnetic due to strong atomic thermal motion causing the disappearance of exchange interaction between coupled atomic magnetic moments. As the temperature decreases below the Curie temperature, the exchange interaction reemerges, resulting in atomic magnetic moments of titanomagnetites retaining a statistically preferred orientation parallel to the paleomagnetic field due to shape anisotropy (Butler, 1992; Stacey & Banerjee, 1974).

Thermogeochronological investigations of the widespread transcurrent tectonics in the region have revealed latest Carboniferous muscovites and biotites $^{40}Ar/^{39}Ar$ cooling ages with closure temperatures ranging from 330 to 425°C (e.g., Grove & Harrison, 1996; Hames & Bowring, 1994; He et al., 2021; Kelley & Platt, 1999; Yin & Nie, 1996). As the Curie temperature of studied titanomagnetite is around 400°C, the transcurrent tectonics was capable of thermally remagnetizing the Baluntai migmatites. In a scenario where the Baluntai migmatites were buried deeper than ∼16 km with ambient temperature exceeding ∼400°C, the transcurrent tectonics would have triggered the exhumation of migmatites, and the magnetic remanences would have been acquired for the first time during this exhumation as the ambient temperature decreased below the Curie temperature of studied titanomagnetites. In this context, the magnetic remanences are theoretically primary but significantly younger than the magnetic fabrics.

Although temperatures may have reached 300–400°C during the magnetization or remagnetization of the Baluntai migmatites, no obvious dynamic recrystallization (such as bulging or sub-grain rotation of quartz) was observed in the leucosomes and mesosomes (Figures 4a–4d; Stipp et al., 2002), and the deformation found in melanosomes should have been inherited from the protoliths and/or paleosome (Figures 4e and 4f). It has been suggested that the boundary conditions of dislocation creep include temperature, differential stress, strain rates, and water content (Hirth & Tullis, 1992; Stipp et al., 2002). In the Baluntai case, even though the temperature condition was met, no significant dynamic recrystallization occurred probably due to the absence of differential stress. As the LPO of biotites of Baluntai migmatites has not significantly changed, the migmatites should have retained their primary magnetic fabrics.

In summary, while the Baluntai migmatites acquired their magnetic fabrics during the migmatization process, the ChRMs resulted from magnetization or remagnetization after the acquisition of magnetic fabrics at ∼314–303 Ma. This case illustrates that primary magnetic fabrics do not necessarily imply contemporaneous magnetic remanences. Our study provides an important, yet rarely reported, example of rocks carrying primary magnetic fabrics while their magnetic remanences are secondary (or at least non-contemporaneous).

5.4. The Practicability of Migmatites in Magnetic Fabric and Paleomagnetic Studies

Despite the structural and compositional complexities, a relatively straightforward magnetic fabric pattern is observed in the Baluntai migmatites. The well-grouped magnetic foliations and disperse lineations reveal an originally horizontal fabric that formed during the migmatization process under a stable tectonic stage (Figure 8). The presence of the Early Carboniferous Wuwamen-Gulougou ophiolites (334–332 Ma; Jiang et al., 2014; Figure 1b) suggests that the Central Tianshan was separated from the Tarim Block during the Early Carboniferous (Wang et al., 2018). Additionally, large-scale strike-slip movements occurred in and around the Central Tianshan from the end of Carboniferous to the Permian (He et al., 2021; Li et al., 2017; P. F. Li et al., 2020; Yin & Nie, 1996). Thus, it can be inferred that the Baluntai migmatites formed in a transition stage between convergence and transcurrent settings, indicating that the convergence and amalgamation of the Central Tianshan with the South Tianshan/Tarim Block had ceased at least by the end of Carboniferous (~314–303 Ma).

The magnetization/remagnetization process of the Baluntai migmatites occurred after the migmatization process. Thermogeochronologic results from various minerals (e.g., monazite, muscovite, and biotite) indicate a rapid exhumation of the migmatites in the Baluntai area at ~310 Ma (Zhu, 2020). This exhumation coincides with the onset of large-scale strike-slip movements in the Baluntai area and the entire Tianshan region (He et al., 2021; Laurent-Charvet et al., 2003; Rolland et al., 2013; Wang et al., 2007; Zhu et al., 2019, 2023). Therefore, the transcurrent tectonics likely triggered the exhumation and associated tilting of the Baluntai migmatites. When the migmatites cooled down through the blocking temperature of titanomagnetite, it recorded the latest Carboniferous paleomagnetic field. Subsequently, the migmatites experienced tilting, most likely by ~10°–20°SW-down, leading to their present occurrence. If this hypothesis is correct, the latest Carboniferous paleomagnetic declination of the Central Tianshan would resemble that of the Tarim Block (e.g., Fang et al., 1996), reinforcing the idea that these blocks were welded together by the end of Carboniferous. Furthermore, their paleomagnetic declination notably differs from that of the Yili Block (up to 60°), which was interpreted as a result of large-scale dextral strike-slip movement along the Nalati Fault from the late Carboniferous to the end Permian (Wang et al., 2007; Zhu et al., 2018).

Based on our study, magnetic fabric analysis of migmatites can unveil the formation process of migmatites and provide insights into regional tectonic evolution. Moreover, while challenging, paleomagnetic study on migmatites has the potential to yield geological meaningful ChRMs once the relationship is understood between the migmatitic foliation and the paleo-plane where magnetic remanences were obtained. In conclusion, migmatites are practical materials for magnetic fabric and paleomagnetic research.

Data Availability Statement

The supporting data for Figures 5–10, the Supporting Information S1 of Tables S1-S4, and Excel Macro "EPMA dating" (Pommier et al., 2003) for monazite age calculation can be found in the website https://doi.org/10.6084/m9.figshare.25674963.v3.

Acknowledgments
We sincerely thank Prof. Kenneth P. Kodama and another anonymous reviewer, and the editor, Dr. Mark Dekkers, together with an expert associate editor for their constructive comments and suggestions that have significantly improved this manuscript. Prof. Yongxiang Li, Drs. Zheng Gong and Xuzhi Hu are also thanked for their help in the AARM investigation. This study was co-sponsored by the National Natural Science Foundation of China (42161144013, 42202234) and China Postdoctoral Science Foundation (2021M692606). The Youth Innovation Team of Shaanxi Universities, the MOST Special Fund from the State Key Laboratory of Continental Dynamics, Northwest University, and the China Scholarship Council (201806190163) are appreciated.

References

Alexeiev, D. V., Biske, Y. S., Wang, B., Djenchuraeva, A. V., Getman, O. F., Aristov, V. A., et al. (2015). Tectono-stratigraphic framework and Palaeozoic evolution of the Chinese South Tianshan. *Geotectonics*, *49*(2), 93–122. https://doi.org/10.1134/S0016852115020028

Allen, M. B., Windley, B. F., & Zhang, C. (1993). Palaeozoic collisional tectonics and magmatism of the Chinese Tien Shan, central Asia. *Tectonophysics*, *220*(1–4), 89–115. https://doi.org/10.1016/0040-1951(93)90225-9

Artemieva, I. M., & Shulgin, A. (2019). Making and altering the crust: A global perspective on crustal structure and evolution. *Earth and Planetary Science Letters*, *512*, 8–16. https://doi.org/10.1016/j.epsl.2019.01.033

Bai, Y. H., Chen, G. L., Sun, Q. G., Sun, Y. H., Li, Y. G., Dong, Y. J., & Sun, D. J. (1987). Late Paleozoic polar wander path for the Tarim platform and its tectonic significance. *Tectonophysics*, *139*(1-2), 145–153. https://doi.org/10.1016/0040-1951(87)90203-4

Bian, W. W., Yang, T. S., Wang, S., Peng, W. X., Zhang, S. H., Wu, H. C., et al. (2022). Cretaceous paleomagnetic and detrital zircon U– Pb geochronological results from the Tethyan Himalaya: Constraints on the Neo-Tethys evolution. *Global and Planetary Change*, *216*, 103903. https://doi.org/10.1016/j.gloplacha.2022.103903

Biedermann, A. R., Pettke, T., Angel, R. J., & Hirt, A. M. (2016). Anisotropy of magnetic susceptibility in alkali feldspar and plagioclase. *Geophysical Journal International*, *205*(1), 479–489. https://doi.org/10.1093/gji/ggw042

Borradaile, G. J., & Henry, B. (1997). Tectonic applications of magnetic susceptibility and its anisotropy. *Earth-Science Reviews*, *42*(1–2), 49–93. https://doi.org/10.1016/S0012-8252(96)00044-X

Borradaile, G. J., Keeler, W., Alford, C., & Sarvas, P. (1987). Anisotropy of magnetic susceptibility of some metamorphic minerals. *Physics of the Earth and Planetary Interiors*, *48*(1–2), 161–166. https://doi.org/10.1016/0031-9201(87)90119-1

Borradaile, G. J., & Werner, T. (1994). Magnetic anisotropy of some phyllosilicates. *Tectonophysics*, *235*(3), 223–248. https://doi.org/10.1016/0040-1951(94)90196-1

Brune, J. N., Henyey, T. L., & Roy, R. F. (1969). Heat flow, stress and rate of slip along the San Andreas fault, California. *Journal of Geophysical Research*, *74*(15), 3821–3827. https://doi.org/10.1029/jb074i015p03821

Butler, R. F. (1992). *Paleomagnetism: Magnetic domains to geologic terranes*. Blackwell Scientific Publications.

Carroll, A. R., Graham, S. A., Hendrix, M. S., Ying, D., & Zhou, D. (1995). Late Palaeozoic tectonic amalgamation of NW China: Sedimentary records of the northern Tarim, northwestern Turpan, and southern Junggar basins. *Geological Society of America Bulletin*, *107*(5), 571–594. https://doi.org/10.1130/0016-7606(1995)107<0571:LPTAON>2.3.CO;2

Chadima, M., & Jelínek, V. (2008). Anisoft 4.2—Anisotropy data browser. *Contributions to Geophysics and Geodesy*, *38*, 41. Special Issue.

Charles, N., Michel, F., & Chen, Y. (2009). The Montagne Noire migmatitic dome emplacement (French Massif central): New insights from Petrofabric and AMS studies. *Journal of Structural Geology*, *31*(11), 1423–1440. https://doi.org/10.1016/j.jsg.2009.08.007

Charvet, J., Shu, L. S., & Laurent-Charvet, S. (2007). Palaeozoic structural and geodynamic evolution of eastern Tianshan (NW China): Welding of the Tarim and Junggar plates. *Episodes*, *30*, 162–186. https://doi.org/10.1007/s00254-007-0834-3

Charvet, J., Shu, L. S., Laurent-Charvet, S., Wang, B., Faure, M., Cluzel, D., et al. (2011). Palaeozoic tectonic evolution of the Tianshan belt, NW China. Science in China, ser. D. *Earth Sciences*, *54*(2), 166–184. https://doi.org/10.1007/s11430-010-4138-1

Chen, X. Y., Wang, Y. J., Sun, L. H., & Fan, W. M. (2009). Zircon SHRIMP U–Pb dating of the granitic gneisses from Bingdaban and Laer-dundaban (Tianshan Orogen) and their geological significances. *Geochimica*, *38*, 424–431. https://doi.org/10.1016/S1874-8651(10)60080-4

Chen, Y., Xu, B., Zhan, S., & Li, Y. A. (2004). First mid-Neoproterozoic paleomagnetic results from the Tarim basin (NW China) and their geodynamic implications. *Precambrian Research*, *133*(3–4), 271–281. https://doi.org/10.1016/j.precamres.2004.05.002

Cheng, X., Wei, B. T., Jiang, N., Zhou, Y. N., Kravchinsky, V. A., Chen, Q. L., et al. (2023). Evolution of the North Qiangtang block in the late Paleozoic: Paleomagnetism and its tectonic implications. *Geological Society of America Bulletin*, *136*(1–2), 707–724. https://doi.org/10.1130/B36825.1

Cocherie, A., Legendre, O., Peucat, J. J., & Kouamelan, A. N. (1998). Geochronology of polygenetic monazites constrained by in situ electron microprobe Th-U-total lead determination: Implications for lead behaviour in monazite. *Geochimica et Cosmochimica Acta*, *62*(14), 2475–2497. https://doi.org/10.1016/S0016-7037(98)00171-9

Cogné, J. P. (2003). PaleoMac: A MacintoshTM application for treating paleomagnetic data and making plate reconstructions. *Geochemistry, Geophysics, Geosystems*, *4*(1), 1007. https://doi.org/10.1029/2001GC000227

D'Agrella-Filho, M. S., Raposo, M. I. B., & Egydio-Silva, M. (2004). Paleomagnetic study of the Juiz de Fora Complex, SE Brazil: Implications for Gondwana. *Gondwana Research*, *7*(1), 103–113. https://doi.org/10.1016/S1342-937X(05)70309-9

Deenen, M. H. L., Langereis, C. G., Van Hinsbergen, D. J. J., & Biggin, A. J. (2011). Geomagnetic secular variation and the statistics of palaeomagnetic directions. *Geophysical Journal International*, *186*(2), 509–520. https://doi.org/10.1111/j.1365-246X.2011.05050.x

Dong, Y. P., Zhang, G. W., Neubauer, F., Liu, X. M., Hauzenberger, C., Zhou, D. W., & Li, W. (2011). Syn- and post-collisional Granitoids in the central Tianshan Orogen: Geochemistry, geochronology and implications for tectonic evolution. *Gondwana Research*, *20*(2–3), 568–581. https://doi.org/10.1016/j.gr.2011.01.013

Dunlop, D. J. (2002). Theory and application of the Day plot (Mrs/Ms versus Hcr/Hc): 2. Application to data for rocks, sediments, and soils. *Journal of Geophysical Research*, *107*(B3), 2057. https://doi.org/10.1029/2001JB000487

Etheridge, M. A. (1983). Differential stress magnitudes during regional deformation and metamorphism: Upper bound imposed by tensile fracturing. *Geology*, *11*(4), 231–234. https://doi.org/10.1130/0091-7613(1983)11<231:dsmdrd>2.0.co;2

Fang, D. J., Jin, G. H., Jiang, L. P., Wang, P. Y., & Wang, Z. L. (1996). Paleozoic paleomagnetic results and the tectonic significance of Tarim plate. *Chinese Journal of Geophysics*, *39*(4), 522–532.

Ferré, E., Teyssier, C., Jackson, M., Thill, J. W., & Rainey, E. S. G. (2003). Magnetic susceptibility anisotropy: A new petrofabric tool in migmatites. *Journal of Geophysical Research*, *108*(B2), 2086. https://doi.org/10.1029/2002JB001790

Ferré, E. C., Martín-Hernández, F., Teyssier, C., & Jackson, M. (2004). Paramagnetic and ferromagnetic anisotropy of magnetic susceptibility in migmatites: Measurements in high and low fields and kinematic implications. *Geophysical Journal International*, *157*(3), 1119–1129. https://doi.org/10.1111/j.1365-246X.2004.02294.x

Fialko, Y., Rivera, L., & Kanamori, H. (2005). Fast track paper: Estimate of differential stress in the upper crust from variations in topography and strike along the san Andreas fault. *Geophysical Journal International*, *160*(2), 527–532. https://doi.org/10.1111/j.1365-246x.2004.02511.x

Fisher, R. (1953). Dispersion on a sphere. *Proceedings of the Royal Society of London, Series A: Mathematical and Physical Sciences*, *217*(1130), 295–305. https://doi.org/10.1098/rspa.1953.0064

Gao, J., He, G. Q., Li, M. S., Xiao, X. C., Tang, Y. Q., Wang, J., & Zhao, M. (1995). The mineralogy, petrology, metamorphic PTDt trajectory and exhumation mechanism of blueschists, South Tianshan, northwestern China. *Tectonophysics*, *250*(1–3), 151–168. https://doi.org/10.1016/0040-1951(95)00026-6

Gao, J., Klemd, R., Qian, Q., Zhang, X., Li, J., Jiang, T., & Yang, Y. Q. (2011). The collision between the Yili and Tarim blocks of the southwestern Altaids: Geochemical and age constraints of a leucogranite dike crosscutting the HP–LT metamorphic belt in the Chinese Tianshan orogen. *Tectonophysics*, *499*(1–4), 118–131. https://doi.org/10.1016/j.tecto.2011.01.001

Gao, J., Li, M., Xiao, X., Tang, Y., & He, G. (1998). Paleozoic tectonic evolution of the Tianshan Orogen, Northwestern China. *Tectonophysics*, *287*(1–4), 213–231. https://doi.org/10.1016/S0040-1951(98)80070-X

Girdler, R. W. (1961). The measurement and computation of anisotropy of magnetic susceptibility in rocks. *Geophysical Journal International*, *5*(1), 34–44. https://doi.org/10.1111/j.1365-246X.1961.tb02927.x

Grove, M., & Harrison, T. M. (1996). 40Ar* diffusion in Fe-rich biotite. *American Mineralogist*, *81*(7–8), 940–951. https://doi.org/10.2138/am-1996-7-816

Hames, W. E., & Bowring, S. A. (1994). An empirical evaluation of the argon diffusion geometry in muscovite. *Earth and Planetary Science Letters*, *124*(1–4), 161–167. https://doi.org/10.1016/0012-821X(94)00079-4

Han, B. F., Guo, Z. J., Zhang, Z. C., Zhang, L., Chen, J. F., & Song, B. (2010). Age, geochemistry, and tectonic implications of a late Paleozoic stitching pluton in the North Tian Shan suture zone, Western China. *Geological Society of America Bulletin*, *122*(3–4), 627–640. https://doi.org/10.1130/B26491.1

Han, B. F., He, G. Q., Wang, X. C., & Guo, Z. J. (2011). Late Carboniferous collision between the Tarim and Kazakhstan–Yili terranes in the Western segment of the South Tian Shan orogen, central Asia, and implications for the northern Xinjiang, western China. *Earth-Science Reviews*, *109*(3–4), 74–93. https://doi.org/10.1016/j.earscirev.2011.09.001

Han, Y. G., & Zhao, G. C. (2018). Final amalgamation of the Tianshan and Junggar orogenic collage in the southwestern central Asian orogenic belt: Constraints on the closure of the paleo-Asian ocean. *Earth-Science Reviews*, *186*, 129–152. https://doi.org/10.1016/j.earscirev.2017.09.012

Hanks, T. C. (1977). Earthquake stress drops, ambient tectonic stresses and stresses that drive plate motions. *Pure and Applied Geophysics*, *115*(1–2), 441–458. https://doi.org/10.1007/bf01637120

He, Z. Y., Wang, B., Ni, X. H., De Grave, J., Scaillet, S., Chen, Y., et al. (2021). Structural and kinematic evolution of strike-slip shear zones around and in the Central Tianshan: Insights for eastward tectonic wedging in the Southwest Central Asian Orogenic Belt. *Journal of Structural Geology*, *144*, 104279. https://doi.org/10.1016/j.jsg.2021.104279

He, Z. Y., Wang, B., Zhong, L. L., & Zhu, X. Y. (2018). Crustal evolution of the Central Tianshan Block: Insights from zircon U-Pb isotopic and structural data from meta-sedimentary and meta-igneous rocks along the Wulasitai—Wulanmoren shear zone. *Precambrian Research*, *314*, 111–128. https://doi.org/10.1016/j.precamres.2018.06.003

Hirth, G., & Tullis, J. (1992). Dislocation creep regimes in quartz aggregates. *Journal of Structural Geology*, *14*(2), 145–159. https://doi.org/10.1016/0191-8141(92)90053-Y

Hrouda, F. (1982). Magnetic anisotropy of rocks and its application in geology and geophysics. *Geophysical Surveys*, *5*(1), 37–82. https://doi.org/10.1007/BF01450244

Hrouda, F., & Chadima, M. (2020). Examples of tectonic overprints of magnetic fabrics in rocks of the Bohemian Massif and Western Carpathians. *International Journal of Earth Sciences*, *109*(4), 1321–1336. https://doi.org/10.1007/s00531-019-01786-8

Hu, A. Q., Wei, G. J., Jahn, B. M., & Zhang, J. B. (2010). Formation of the 0.9 Ga Neoproterozoic granitoids in the Tianshan Orogen, NW China: Constraints from the SHRIMP zircon age determination and its tectonic significance. *Geochimica*, *39*, 197–212. https://doi.org/10.1017/S0004972710001772

Huang, B. C., Piper, J. D. A., Sun, L. S., & Zhao, Q. (2019). New paleomagnetic results for Ordovician and Silurian rocks of the Tarim Block, Northwest China and their paleogeographic implications. *Tectonophysics*, *755*, 91–108. https://doi.org/10.1016/j.tecto.2019.02.010

Huang, B. C., Yan, Y. G., Piper, J. D. A., Zhang, D. H., Yi, Z. Y., Yu, S., & Zhou, T. H. (2018). Paleomagnetic constraints on the paleogeography of the East Asian blocks during late Paleozoic and early Mesozoic times. *Earth-Science Reviews*, *186*, 8–36. https://doi.org/10.1016/j.earscirev.2018.02.004

Jackson, M. J., Banerjee, S. K., Marvin, J. A., Lu, R., & Gruber, W. (1991). Detrital remanence inclination errors and anhysteretic remanence anisotropy: Quantitative model and experimental results. *Geophysical Journal International*, *104*(1), 95–103. https://doi.org/10.1111/j.1365-246X.1991.tb02496.x

Jahn, B. M., Wu, F. Y., & Chen, B. (2000). Granitoids of the central Asian orogenic belt and continental growth in the Phanerozic. *GSA Special Papers*, *350*, 181–193. https://doi.org/10.1130/0-8137-2350-7.181

Jiang, T., Gao, J., Klemd, R., Qian, Q., Zhang, X., Xiong, X. M., et al. (2014). Paleozoic ophiolitic mélanges from the South Tianshan orogen, NW China: Geological, geochemical and geochronological implications for the geodynamic setting. *Tectonophysics*, *612–613*, 106–127. https://doi.org/10.1016/j.tecto.2013.11.038

Jing, X. Q., Yang, Z. Y., Tong, Y. B., & Han, Z. R. (2015). A revised paleomagnetic pole from the mid-Neoproterozoic Liantuo Formation in the Yangtze block and its paleogeographic implications. *Precambrian Research*, *268*, 194–211. https://doi.org/10.1016/j.precamres.2015.07.007

Johnson, C. L., Constable, C. G., Tauxe, L., Barendregt, R., Brown, L. L., Coe, R. S., et al. (2008). Recent investigations of the 0–5 Ma geomagnetic field recorded by lava flows. *Geochemistry, Geophysics, Geosystems*, *9*(4), Q04032. https://doi.org/10.1029/2007GC001696

Kelley, S. P., & Platt, J. P. (1999). Ar-Ar dating of biotite and muscovite from Alboran basement samples. *Site*, *976*, 1999. https://doi.org/10.2973/odp.proc.sr.161.215.1999

Kirschvink, J. L. (1980). The least squares line and the analysis of paleomagnetic data. *Geophysical Journal International*, *62*(3), 699–718. https://doi.org/10.1111/j.1365246X.1980.tb02601.x

Kligfield, R., Lowrie, W., Hirt, A., & Siddans, A. W. B. (1983). Effect of progressive deformation on remanent magnetization of Permian Redbeds from the Alpes Maritimes (France). *Tectonophysics*, *97*(1–2), 59–85. https://doi.org/10.1016/0040-1951(83)90211-1

Kodama, K. P. (1997). A successful rock magnetic technique for correcting paleomagnetic inclination shallowing: Case study of the Nacimiento formation, New Mexico. *Journal of Geophysical Research*, *102*, 5193–5206. https://doi.org/10.1029/96JB03833

Kruckenberg, S. C., Ferré, E. C., Teyssier, C., Vanderhaeghe, O., Whitney, D. L., Seaton, N. C. A., & Skord, J. A. (2010). Viscoplastic flow in migmatites deduced from fabric anisotropy: An example from the Naxos dome, Greece. *Journal of Geophysical Research*, *115*(B9), B09401. https://doi.org/10.1029/2009JB007012

Laurent-Charvet, S., Charvet, J., Monié, P., & Shu, L. S. (2003). Late Paleozoic strike-slip shear zones in Eastern Central Asia (NW China): New structural and geochronological data. *Tectonics*, *22*(2), 1009. https://doi.org/10.1029/2001TC901047

Lei, R. X., Wu, C. Z., Gu, L. X., Zhang, Z. Z., Chi, G. X., & Jiang, Y. H. (2011). Zircon U–Pb chronology and Hf isotope of the Xingxingxia granodiorite from the central Tianshan zone (NW China): Implications for the tectonic evolution of the Southern Altaids. *Gondwana Research*, *20*(2–3), 582–593. https://doi.org/10.1016/j.gr.2011.02.010

Li, P. F., Sun, M., Rosenbaum, G., Cai, K. D., Yuan, C., Jourdan, F., et al. (2020a). Tectonic evolution of the Chinese Tianshan Orogen from subduction to arc-continent collision: Insight from polyphase deformation along the Gangou section, Central Asia. *Geological Society of America Bulletin*, *132*(11–12), 2529–2552. https://doi.org/10.1130/B35353.1

Li, P. F., Sun, M., Rosenbaum, G., Jourdan, F., Li, S., & Cai, K. D. (2017). Late Paleozoic closure of the Ob-Zaisan ocean along the Irtysh shear zone (NW China): Implications for arc amalgamation and oroclinal bending in the central Asian orogenic belt. *Geological Society of America Bulletin*, *129*(5–6), 547–569. https://doi.org/10.1130/b31541.1

Li, S. H., Van Hinsbergen, D. J. J., Shen, Z. S., Najman, Y., Deng, C. L., & Zhu, R. X. (2020b). Anisotropy of Magnetic Susceptibility (AMS) analysis of the Gonjo Basin as an independent constraint to date Tibetan shortening pulses. *Geophysical Research Letters*, *47*(8), e2020GL087531. https://doi.org/10.1029/2020GL087531

Li, Y. X., & Kodama, K. P. (2016). Detecting and correcting for paleomagnetic inclination shallowing of sedimentary rocks: A review. *Frontiers of Earth Science*, *4*, 7. https://doi.org/10.3389/feart.2016.00007

Liu, H. S., Liu, L. M., Zhang, D. X., Huang, F. F., & Zhang, X. (2023). Unilateral magma emplacement of the Telimbela batholith in the central Ecuadorian arc: Implications for kinematics of oblique subduction of the Farallon-Nazca plate. *Tectonics*, *42*(2), e2021TC007114. https://doi.org/10.1029/2021TC007114

Liu, H. S., Wang, B., Shu, L. S., Jahn, B. M., & Lizuka, Y. (2014). Detrital zircon ages of Proterozoic meta-sedimentary rocks and Paleozoic sedimentary cover of the northern Yili block: Implications for the tectonics of microcontinents in the central Asian orogenic belt. *Precambrian Research*, *252*, 209–222. https://doi.org/10.1016/j.precamres.2014.07.018

Liu, J. S., Wang, B., Ni, X. H., Song, F., Sun, Z. C., Deng, J., & Li, Y. Y. (2022). Late Devonian transition from advancing to retreating subduction in the SW Central Asian Orogenic Belt: Insights from multiple deformation and magmatic events in the southern Yili Block, NW China. *Gondwana Research*, *105*, 468–487. https://doi.org/10.1016/j.gr.2021.10.001

Ma, X. X., Shu, L. S., Jahn, B.-M., Zhu, W. B., & Faure, M. (2012). Precambrian tectonic evolution of Central Tianshan, NW China: Constraints from U-Pb dating and in situ Hf isotopic analysis of detrital zircons. *Precambrian Research*, *222–223*, 450–473. https://doi.org/10.1016/j.precamres.2011.06.004

Ma, X. X., Shu, L. S., Meert, J. G., & Li, J. Y. (2014). The Paleozoic evolution of central Tianshan: Geochemical and geochronological evidence. *Gondwana Research*, *25*(2), 797–819. https://doi.org/10.1016/j.gr.2013.05.015

McCabe, C., Jackson, M., & Ellwood, B. B. (1985). Magnetic anisotropy in the Trenton limestone: Results of a new technique, anisotropy of anhysteretic susceptibility. *Geophysical Research Letters*, *12*(6), 333–336. https://doi.org/10.1029/GL012i006p00333

McElhinny, M. W. (1964). Statistical significance of the fold test in palaeomagnetism. *Geophysical Journal International*, *8*(3), 338–340. https://doi.org/10.1111/j.1365-246X.1964.tb06300.x

McFadden, P. L., & McElhinny, M. W. (1990). Classification of the reversal test in paleomagnetism. *Geophysical Journal International*, *103*(3), 725–729. https://doi.org/10.1111/j.1365-246X.1990.tb05683.x

McGarr, A., & Gay, N. C. (1978). State of stress in the earth's crust. *Annual Review of Earth and Planetary Sciences*, *6*(1), 405–436. https://doi.org/10.1146/annurev.ea.06.050178.002201

Meng, Z. F. (1991). Palaeomagnetic study of upper Palaeozoic erathem along the southwestern margin of Tarim block, China. *Acta Sedimentologica Sinica*, *9*, 105–109.

Mitchell, R. N., Zhang, N., Salminen, J., Liu, Y. B., Spencer, C. J., Steinberger, B., et al. (2021). The supercontinent cycle. *Nature Reviews Earth & Environment*, *2*(5), 358–374. https://doi.org/10.1038/s43017-021-00160-0

Molnar, P., & England, P. (1990). Temperatures, heat flux, and frictional stress near major thrust faults. *Journal of Geophysical Research*, *95*(B4), 4833–4856. https://doi.org/10.1029/jb095ib04p04833

Nagata, T. (1961). *Rock magnetism*. Maruzen Ltd.

Ni, X. H., Wang, B., Cluzel, D., Liu, J. S., & He, Z. Y. (2021). Late Paleozoic tectonic evolution of the North Tianshan Belt: New structural and geochronological constraints from meta-sedimentary rocks and migmatites in the Harlik Range (NW China). *Journal of Asian Earth Sciences*, *210*, 104711. https://doi.org/10.1016/j.jseaes.2021.104711

Patzelt, A., Li, H. M., Wang, J. D., & Appel, E. (1996). Palaeomagnetism of cretaceous to Tertiary sediments from southern Tibet: Evidence for the extent of the northern margin of India prior to the collision with Eurasia. *Tectonophysics*, *259*(4), 259–284. https://doi.org/10.1016/0040-1951(95)00181-6

Pe-Piper, G., Kotopouli, C. N., & Piper, D. J. W. (1997). Granitoid rocks of Naxos, Greece: Regional geology and petrology. *Geological Journal*, *32*(2), 153–171. https://doi.org/10.1002/(SICI)1099-1034(199706)32:2<153::AID-GJ737>3.0.CO;2-1

Pesonen, L. J., Evans, D. A. D., Veikkolainen, T., Salminen, J., & Elming, S. K. (2021). Precambrian supercontinents and supercycles—An overview. *Sciencdirect. Ancient Supercontinents and the Paleogeography of Earth*, 1–50. https://doi.org/10.1016/B978-0-12-818533-9.00020-5

Poirier, J.-P. (1985). *Creep of crystals — high-temperature deformation processes in Metals, ceramics and minerals*. Cambridge University Press.

Pommier, A., Cocherie, A., & Legendre, O. (2003). EPMA dating: A program for age calculation from electron microprobe measurements of U-Th-Pb. In EGU2003 [Software]. *Figshare*. https://doi.org/10.6084/m9.figshare.25674963.v3

Randall, R. P. (1990). U–Pb dating of monazite and its application to geological problems. *Canadian Journal of Earth Sciences*, *27*(11), 1431–1450. https://doi.org/10.1139/e90-152

Raposo, M. I. B., D'Agrella-Filho, M. S., & Siqueira, R. (2003). The effect of magnetic anisotropy on paleomagnetic directions in high-grade metamorphic rocks from the Juiz de Fora Complex, SE Brazil. *Earth and Planetary Science Letters*, *209*, 131–147. https://doi.org/10.1016/S0012-821X(03)00065-7

Rochette, P. (1987). Magnetic susceptibility of the rock matrix related to magnetic fabric studies. *Journal of Structural Geology*, *9*(8), 1015–1020. https://doi.org/10.1016/0191-8141(87)90009-5

Rochette, P., Jackson, M., & Aubourg, C. (1992). Rock magnetism and the interpretation of anisotropy of magnetic susceptibility. *Review of Geophysics*, *30*(3), 209–226. https://doi.org/10.1029/92RG00733

Rolland, Y., Alexeiev, D. V., Kröner, A., Corsini, M., Loury, C., & Monié, P. (2013). Late Palaeozoic to Mesozoic kinematic history of the Talas–Ferghana strike-slip fault (Kyrgyz West Tianshan) as revealed by $^{40}Ar/^{39}Ar$ dating of syn-kinematic white mica. *Journal of Asian Earth Sciences*, *67*, 76–92. https://doi.org/10.1016/j.jseaes.2013.02.012

Saxov, S., & Abrahamsen, N. (1964). Some rock densities in Bornholm. *Geologiska Foreningen i Stockholm Forhandlingar*, *86*(1), 83–95. https://doi.org/10.1080/11035897.1964.9626368

Schulmann, K., Edel, J., Hasalová, P., Cosgrove, J., Ježek, J., & Lexa, O. (2009). Influence of melt induced mechanical anisotropy on the magnetic fabrics and rheology of deforming migmatites, Central Vosges, France. *Journal of Structural Geology*, *31*(10), 1223–1237. https://doi.org/10.1016/j.jsg.2009.07.004

Sengör, A. M. C., Natal'in, B. A., & Burtman, V. S. (1993). Evolution of the Altaid tectonic collage and Palaeozoic crustal growth in Eurasia. *Nature*, *364*(6435), 299–307. https://doi.org/10.1038/364299a0

Shi, W. X., Liao, Q. A., Hu, Y. Q., & Yang, Z. F. (2010). Characteristics of mesoproterozoic granites and their geological significances from middle Tianshan block, East Tianshan District, NW China. *Geological Science and Technology Information*, *29*, 29–37. https://doi.org/10.1017/S0004972710001772

Shu, L. S., Deng, X. L., Zhu, W. B., Ma, D. S., & Xiao, W. J. (2011). Precambrian tectonic evolution of the Tarim block, NW China: New geochronological insights from the Quruqtagh domain. *Journal of Asian Earth Sciences*, *42*(5), 774–790. https://doi.org/10.1016/j.jseaes.2010.08.018

Shu, L. S., Yu, J., Charvet, J., Laurent-Charvet, S., Sang, H., & Zhang, R. (2004). Geological, geochronological and geochemical features of Granulites in the Eastern Tianshan, NW China. *Journal of Asian Earth Sciences*, *24*(1), 25–41. https://doi.org/10.1016/j.jseaes.2003.07.002

Southwick, D. L., & Chandler, V. W. (1996). Block and shear-zone architecture of the Minnesota river valley Subprovince: Implications for late Archean accretionary tectonics. *Canadian Journal of Earth Sciences*, *33*(6), 831–847. https://doi.org/10.1139/e96-063

Stacey, F. D., & Banerjee, S. K. (1974). *The physical principles of rock magnetism*. Elsevier.

Stipp, M., Sünitz, H., Heilbronner, R., & Schmid, S. M. (2002). The eastern Tonale fault zone: A "natural laboratory" for crystal plastic deformation of quartz over a temperature range from 250 to 700°C. *Journal of Structural Geology*, *24*(12), 1861–1884. https://doi.org/10.1016/S0191-8141(02)00035-4

Sun, Z. M., Pei, J. L., Li, H. B., Xu, W., Jiang, W., Zhu, Z. M., et al. (2012). Palaeomagnetism of late cretaceous sediments from southern Tibet: Evidence for the consistent palaeolatitudes of the southern margin of Eurasia prior to the collision with India. *Gondwana Research*, *21*(1), 53–63. https://doi.org/10.1016/j.gr.2011.08.003

Syono, Y. (1960). Magnetic susceptibility of some rock forming silicate minerals such as amphiboles, Biotites, cordierites and garnets. *Journal of Geomagnetism and Geoelectricity*, *11*(3), 85–93. https://doi.org/10.5636/jgg.11.85

Tarduno, J. A., Cottrell, R. D., Bono, R. K., Rayner, N., Davis, W. J., Zhou, T. H., et al. (2023). Hadaean to Palaeoarchaean stagnant-lid tectonics revealed by zircon magnetism. *Nature*, *618*(7965), 531–536. https://doi.org/10.1038/s41586-023-06024-5

Tarling, D., & Hrouda, F. (1993). *Magnetic anisotropy of rocks*. Chapman & Hall.

Torsvik, T. H., Van der Voo, R., Preeden, U., Mac Niocaill, C., Steinberger, B., Doubrovine, P. V., et al. (2012). Phanerozoic polar wander, palaeogeography and dynamics. *Earth-Science Reviews*, *114*(3–4), 325–368. https://doi.org/10.1016/j.earscirev.2012.06.007

Twiss, R. J. (1977). Theory and applicability of a recrystallized grainsize palaeopiezometer. *Pure and Applied Geophysics*, *115*(1–2), 227–244. https://doi.org/10.1007/bf01637105

Wang, B., Chen, Y., Zhan, S., Shu, L., Faure, M., Cluzel, D., & Laurent-Charvet, S. (2007). Primary carboniferous and Permian paleomagnetic results from the Yili block (NW China) and their implications on the geodynamic evolution of Chinese Tianshan belt. *Earth and Planetary Science Letters*, *263*(3–4), 288–308. https://doi.org/10.1016/j.epsl.2007.08.037

Wang, B., Faure, M., Cluzel, D., Shu, L. S., Charvet, J., Meffre, S., & Ma, Q. (2006). Late Paleozoic tectonic evolution of the Northern West Chinese Tianshan belt. *Geodinamica Acta*, *19*(3–4), 237–247. https://doi.org/10.3166/ga.19.237-247

Wang, B., Faure, M., Shu, L., Cluzel, D., Charvet, J., De Jong, K., & Chen, Y. (2008). Paleozoic tectonic evolution of the Yili block, western Chinese Tianshan. *Bull. Soc. Geol. France*, *179*(5), 483–490. https://doi.org/10.2113/gssgfbull.179.5.483

Wang, B., Liu, H. S., Shu, L. S., Jahn, B. M., Chung, S. L., Zhai, Y. Z., & Liu, D. Y. (2014). Early neoproterozoic crustal evolution in northern Yili block: Insightsfrom migmatite, orthogneiss and leucogranite of the Wenquan metamorphic complex in the NW Chinese Tianshan. *Precambrian Research*, *242*, 58–81. https://doi.org/10.1016/j.precamres.2013.12.006

Wang, B., Shu, L., Faure, M., Jahn, B. M., Cluzel, D., Charvet, J., et al. (2011). Paleozoic tectonics of the southern Chinese Tianshan: Insights from structural, chronological and geochemical studies of the Heiyingshan ophiolitic mélange (NW China). *Tectonophysics*, *497*(1–4), 85–104. https://doi.org/10.1016/j.tecto.2010.11.004

Wang, B., Song, F., Ni, X. H., Cao, T. T., Liu, J. S., Zhong, L. L., et al. (2022). Paleozoic accretionary orogenesis and major transitional tectonic events of the Tianshan orogen. *Acta Geologica Sinica*, *96*(10), 3514–3540. https://doi.org/10.19762/j.cnki.dizhixuebao.2022081

Wang, B., Zhai, Y. Z., Kapp, P., de Jong, K., Zhong, L. L., Liu, H. S., et al. (2018). Accretionary tectonics of back-arc oceanic basins in the South Tianshan: Insights from structural, geochronological, and geochemical studies of the Wuwamen ophiolite Melange. *Geological Society of America Bulletin*, *130*(1–2), 284–306. https://doi.org/10.1130/b31397.1

Wang, S., Yang, T. S., Gao, F., Bian, W. W., Jin, J. J., Peng, W. X., et al. (2022). Paleomagnetic and geochronological results of the Risong formation in the western Lhasa terrane: Insights into the Lhasa-Qiangtang collision and Stratal age. *Palaeogeogr. Palaeocl.*, *586*, 110778. https://doi.org/10.1016/j.palaeo.2021.110778

Wang, X. S., Klemd, R., Gao, J., Jiang, T., & Zhang, X. (2021). Early devonian tectonic conversion from contraction to extension in the Chinese western tianshan: A response to slab rollback. *Geological Society of America Bulletin*, *133*(7–8), 1613–1633. https://doi.org/10.1130/b35760.1

Wei, W., Lin, W., Chen, Y., Faure, M., Ji, W. B., Hou, Q. L., et al. (2023). Tectonic controls on magmatic tempo in an active continental margin: Insights from the Early Cretaceous syn-tectonic magmatism in the Changle-Nan'ao Belt, South China. *Journal of Geophysical Research*, *128*(2), e2022JB025973. https://doi.org/10.1029/2022JB025973

Wen, B., Li, Y. X., & Zhu, W. B. (2013). Paleomagnetism of the neoproterozoic diamictites of the Qiaoenbrak formation in the Aksu area, NW China: Constraints on the paleogeographic position of the Tarim block. *Precambrian Research*, *226*, 75–90. https://doi.org/10.1016/j.precamres.2012.10.018

Wolfson, R. (2012). Energy from earth and moon. In *Energy, environment, and climate* (2nd ed., pp. 204–224). W.W. Norton & Company.

Wooden, J. L., Goldich, S. S., & Suhr, N. H. (1980). Origin of the Morton gneiss, southwestern Minnesota: Part 2. Geochemistry. *Pediatrics*, 57–76. https://doi.org/10.1130/spe182-p57

Wu, F. Y., Wan, B., Zhao, L., Xiao, W. J., & Zhu, R. X. (2020). Tethys geodynamics. *Acta Petrologica Sinica*, *36*(6), 1627–1674. https://doi.org/10.18654/1000-0569/2020.06.01

XBGMR. (1993). *Regional geology of Xinjiang Uygur autonomy region*. Geological Publishing House.

Xiao, W. J., Windley, B. F., Allen, M. B., & Han, C. M. (2013). Paleozoic multiple accretionary and collisional tectonics of the Chinese Tianshan orogenic collage. *Gondwana Research*, *23*(4), 1316–1341. https://doi.org/10.1016/j.gr.2012.01.012

Xiao, W. J., Windley, B. F., Sun, S., Li, J. L., Huang, B. C., Han, C. M., et al. (2015). A tale of amalgamation of three Permo-Triassic Collage Systems in Central Asia: Oroclines, sutures, and terminal accretion. Annu. *Review of Earth and Planetary Sciences*, *43*(1), 477–507. https://doi.org/10.1146/annurev-earth-060614-105254

Xu, X. Y., Li, R. S., Chen, J. L., Ma, Z. P., Li, Z. P., Wang, H. L., et al. (2014). New constrains on the Paleozoic tectonic evolution of the Northern Xinjiang area. *Acta Petrologica Sinica*, *30*(6), 1521–1534. (in Chinese with English abstract).

Xue, Z. H., Lin, W., Chu, Y., Wei, W., Feng, Z. T., & Zhang, J. F. (2022). Late Triassic successive amalgamation between the South China and North China blocks: Insights from structural analysis and magnetic fabrics study of the Bikou Terrane and its adjacent area, Northwestern Yangtze block, central China. *Geological Society of America Bulletin*, *134*(7–8), 2051–2071. https://doi.org/10.1130/B36228.1

Yang, T. N., Li, J. Y., Sun, G. H., & Wang, Y. B. (2006). Earlier devonian active continental arc in central Tianshan: Evidence of geochemical analyses and zircon SHRIMP dating on mylonitized granitic rock. *Acta Petrologica Sinica*, *22*, 41–48. https://doi.org/10.3321/j.issn:10000569.2006.01.004

Yi, Z. Y., Huang, B. C., Yang, L. K., Tang, X. D., Yan, Y. G., Qiao, Q. Q., et al. (2015). A quasi-linear structure of the southern margin of Eurasia prior to the India-Asia collision: First paleomagnetic constraints from Upper Cretaceous volcanic rocks near the western syntaxis of Tibet. *Tectonics*, *34*(7), 1431–1451. https://doi.org/10.1002/2014TC003571

Yin, A., & Nie, S. Y. (1996). A Phanerozoic palinspastic reconstruction of China and its neighboring regions. In A. Yin & M. Harrison (Eds.), *The tectonic evolution of Asia, Rubey colloquium* (pp. 442–485). Cambridge University Press.

Yuan, J., Deng, C. L., Yang, Z. Y., Krijgsman, W., Qin, H. F., Yi, L., et al. (2023). New paleomagnetic data from the central Tethyan Himalaya refine the size of Greater India during the Campanian. *Earth and Planetary Science Letters*, *622*, 118422. https://doi.org/10.1016/j.epsl.2023.118422

Zapletal, K. (1990). Low-field susceptibility anisotropy of some biotite crystals. *Physics of the Earth and Planetary Interiors*, *63*(1–2), 85–97. https://doi.org/10.1016/0031-9201(90)90063-4

Zhai, Y. J., Zhang, Z. K., Li, Y. A., Li, Q., Li, Y. P., McWilliams, M., et al. (1988). A study of upper carboniferous paleomagnetism for the Tarim block. *Geoscience*, 43–56. (in Chinese with English abstract).

Zhan, S., Chen, Y., Xu, B., Wang, B., & Faure, M. (2007). Late Neoproterozoic paleomagnetic results from the Sugetbrak Formation of the Aksu area, Tarim basin (NW China) and their implications to paleogeographic reconstructions and the snowball Earth hypothesis. *Precambrian Research*, *154*(3–4), 143–158. https://doi.org/10.1016/j.precamres.2007.01.001

Zhang, X., Wang, X. S., Jiang, T., & Gao, J. (2022). Petrogenesis and tectonic setting of the late carboniferous igneous rocks in the Baluntai region of the Chinese western Tianshan. *Earth Science*, *47*(3), 1038–1058. (in chinese with English abstract).

Zhao, J., Dong, Y. P., & Huang, B. C. (2020). Paleomagnetic constraints of the lower triassic strata in south Qinling belt: Evidence for a discrete terrane between the North and South China blocks. *Tectonics*, *39*(3), e2019TC005698. https://doi.org/10.1029/2019TC005698

Zhao, P., Chen, Y., Zhan, S., Xu, B., & Faure, M. (2014). The apparent polar wander path of the Tarim block (NW China) since the neoproterozoic and its implications for a long-term Tarim–Australia connection. *Precambrian Research*, *242*, 39–57. https://doi.org/10.1016/j.precamres.2013.12.009

Zhong, L. L., Wang, B., Alexeiev, D. V., Cao, Y. C., Biske, Y. S., Liu, H. S., et al. (2017). Paleozoic multi-stage accretionary evolution of the SW Chinese Tianshan: New constraints from plutonic complex in the Nalati Range. *Gondwana Research*, *45*, 254–274. https://doi.org/10.1016/j.gr.2016.12.012

Zhong, L. L., Wang, B., de Jong, K., Zhai, Y. Z., & Liu, H. S. (2019). Deformed continental arc sequences in the South Tianshan: New constraintson the early paleozoic accretionary tectonics of the central Asian orogenic belt. *Tectonophysics*, *768*, 228169. https://doi.org/10.1016/j.tecto.2019.228169

Zhong, L. L., Wang, B., Shu, L. S., Liu, H. S., Mu, L. X., Ma, Y. Z., & Zhai, Y. Z. (2015). Structural overprints of early Paleozoic arc-related intrusive rocks in the Chinese central Tianshan: Implications for Paleozoic accretionary tectonics in SW central Asian orogenic belts. *Journal of Asian Earth Sciences*, *113*, 194–217. https://doi.org/10.1016/j.jseaes.2014.12.003

Zhu, X. (2020). *Late Paleozoic paleomagnetic study in the Tianshan and Beishan areas and its constraints on the tectonic and paleogeographic reconstructions of the southern Central Asian Orogenic Belt*. Doctoral dissertation. Nanjing University.

Zhu, X., Chen, Y., Wang, B., Dong, Y. P., Scaillet, S., Faure, M., et al. (2023). Paleomagnetic study on the Early Permian Gubaoquan doleritic dike swarm in the southern Beishan area, NW China: Implications for the tectonic and paleogeographic reconstructions of the southern Central Asian Orogenic Belt. *Journal of Asian Earth Sciences*, *256*, 105832. https://doi.org/10.1016/j.jseaes.2023.105832

Zhu, X., Wang, B., Chen, Y., & Liu, H. (2019). Constraining the intracontinental tectonics of the SW central Asian orogenic belt by the early permian paleomagnetic Pole for the Turfan-Hami block. *Journal of Geophysical Research*, *124*(12), 12366–12387. https://doi.org/10.1029/2019JB017680

Zhu, X., Wang, B., Chen, Y., Liu, H., Horng, C. S., Choulet, F., et al. (2018). First early Permian paleomagnetic pole for the Yili block and its implications for late Paleozoic postorogenic kinematic evolution of the SW central Asian Orogenic Belt. *Tectonics*, *37*(6), 1709–1732. https://doi.org/10.1029/2017TC004642

Zijderveld, J. D. A. (1967). A.C. demagnetization of rocks: Analysis of results. In D. W. Collinson, K. M. Creer, & S. K. Runcorn (Eds.), *Methods on paleomagnetism* (pp. 245–286). Elsevier.